Neurovascular Coupling in the Basolateral Amygdala Modulates Negative Emotions

Jiayu Ruan[1,2,3,4], Xinghua Quan[2,3,4], Yiyi Zhang[2,3,4], Huiqi Xie[2,3,4], Dongdong Zhang[2,3,4], Wentao Wang[2,3,4], Bingrui Zhao[2,3,4], Danping Lu[2,3,4], Jie-Min Jia[2,3,4*]

Affiliations

[1] College of Life Sciences, Zhejiang University, Hangzhou, Zhejiang, China.

[2] Westlake Laboratory of Life Sciences and Biomedicine, Hangzhou, China.

[3] Key Laboratory of Growth Regulation and Translational Research of Zhejiang Province, School of Life Sciences, Westlake University, Hangzhou, China.

[4] Laboratory of Neurovascular Biology, Institute of Basic Medical Sciences, Westlake Institute for Advanced Study, Hangzhou, China.

*Correspondence: jiajiemin@westlake.edu.cn

ABSTRACT

Emotion induces changes in regional cerebral blood flow (rCBF), a manifestation of neurovascular coupling (NVC), yet whether NVC might feedback to modulate emotion actively remains unexplored. Here, we demonstrated that NVC actively modulates stress-induced negative emotions. We established bidirectional manipulations of NVC in freely moving mice by employing integrated pharmacological, genetic, and arteriolar optogenetic approaches. Our results showed that both systemic and basolateral amygdala (BLA) regional specific NVC deficiencies heightened emotional responses when mice transitioned from a home cage to anxiogenic environments, and local restoration of NVC in the BLA normalized these responses. Furthermore, by combining BLA neuronal activity mapping with behavioral measures of responses to various stressors, we revealed that the spatial patterns of BLA neuronal activation predicted emotional response magnitudes, with hyper- and hypoactive BLA predicting heightened and blunted behavioral responses, respectively, in the NVC-deficient mice. Finally, enhancing NVC, achieved through either pharmacological or genetic manipulations, promoted resilience to chronic-stress-induced NVC impairments and alleviated emotional distress. These findings established NVC as an allostatic program for fine-tuning emotional responses, with implications for understanding and treating emotional disorders.

INTRODUCTION

Emotion is a complex, integrative response to changes in internal and external environments.[1] Emotional flexibility—the capacity to dynamically regulate and adapt emotional responses—is fundamental for mental health and, in some contexts, survival.[2] Deficits in this flexibility can lead to emotional rigidity, a hallmark of emotional dysregulation, strongly associated with psychiatric disorders such as Post-Traumatic Stress Disorder and depression.[3, 4] Therefore, understanding the molecular and cellular mechanisms that modulate emotional flexibility and rigidity holds critical implications for elucidating resilience to psychological trauma.[5, 6]

Regional neuronal activity, for example, elicited by emotional challenge, tightly couples with regional cerebral blood flow (rCBF) changes–a phenomenon known as neurovascular coupling (NVC)–which underlies the blood-oxygen-level-dependent (BOLD) signals widely used in functional imaging.[7-10] Traditionally, NVC has been widely viewed as a passive proxy for local neuronal activity.[11] Yet despite decades of investigation into the biophysical mechanisms of NVC, its active role—if any—in modulating neuronal circuit function and behavior remains unresolved. Recent studies suggest that NVC in the hippocampus may influence neurogenesis, hinting at a broader regulatory function beyond its hemodynamic role.[12]

Particularly in emotional processing circuits, does the cerebrovascular

network in emotional centers, such as the basolateral amygdala (BLA), simply mirror changes in neuronal firing during stress, or can it actively gate or tune emotional reactivity? BLA has long been recognized as a central hub for processing negative emotions, with altered neuronal activity—either hyperactivity or hypoactivity—linked to emotional dysfunction.[4, 13] The role of NVC in the BLA in modulating negative emotions, a yet-underexplored regulatory element, represents the focal point of our study.

In this study, using pharmacological, genetic, and arteriolar optogenetic approaches, we demonstrated that NVC in the BLA plays a causal role in modulating stress-induced emotional responses. In contrast, NVC in the somatosensory barrel cortex (S1BF) appeared to be functionally dispensable in this context. Our findings revealed that NVC dysfunction leads to context-inappropriate emotional behaviors—characterized by exaggerated or blunted reactions—reminiscent of bipolar-like emotional responses in emotional rigidity. Conversely, enhancing BLA NVC mitigated negative emotional responses. These results established BLA NVC as an active modulatory mechanism in emotional processing and suggested that targeting NVC may offer novel strategies for treating emotional dysregulation in psychiatric disorders.

RESULTS

Mild and strong stress-induced defecation requires BLA activity

Previous studies have demonstrated that stress activates BLA neurons under both mild and intense conditions, such as in the open field test (OFT) and acute restraint stress (ARS).[14, 15] Additionally, stress induces defecation in rodents, a behavior distinct from normal bowel movements, reflecting emotional responses.[16] This stress-induced defecation has long been considered as one of the indicators of negative emotional states.[17, 18] However, the relationship between stress-induced BLA activity and defecation remains unclear.

To investigate this relationship, we measured BLA neuronal activity and defecation behavior in the same mice under three conditions: home cage (minimal stress), OFTs (mild stress), and ARS (intense stress) (Fig. 1a). OFTs were conducted in arenas of varying sizes (40 cm, 35 cm, and 10 cm) to assess the impact of spatial size as a potential variable. Similar to ARS, OFTs induced stress-induced defecation and c-Fos (a marker of neuronal activity) expression,[14] both of which increased with stress levels (Fig. 1b, c; supplementary information, Fig. S1), showing a strong positive correlation (Fig. 1d).

Surprisingly, subtle differences in stress intensity between the 40 cm and 35 cm OFTs led to a distinct increase in BLA c-Fos expression (Fig. 1b), which is also reflected as decreased time spent in the box's center and extended total

running distance in the 35 cm OFT (Fig. 1e, f), which are two conventional indicators. This phenomenon may be attributed to the smaller arena size (35 cm), which likely induced greater stress in mice by limiting exploratory behavior.[19] Stress-induced defecation successfully differentiated these mild variations in stress levels (Fig. 1c), akin to the above two conventional indicators. These findings supported the perspective that 35 cm OFT induced more stress than 40 cm OFT, and defecation can be a comparably effective measure of stress in mild conditions. Furthermore, defecation locations in the 40 cm OFT (Fig. 1g) exhibited a comparable preference for the peripheral zone, consistent with the typical peripheral zone preference observed in mice (Fig. 1h),[14] further suggesting that stress-induced defecation is a structured and non-random behavior linked to BLA activity.

To further verify this phenomenon, we employed a chemogenetic approach to selectively inhibit excitatory neurons in the BLA by expressing hM4Di receptors (Fig. 1i). This manipulation reduced ARS-induced c-Fos expression in the BLA (Fig. 1j) and significantly suppressed stress-induced defecation in both OFT and ARS (Fig. 1k). Except for defecation bots, we assessed defecation rate (proportion of mice defecating) and latency (time to first pellet) in the OFT. Chemogenetic inhibition reduced the defecation rate and prolonged the defecation latency (Fig. 1l), while no changes were observed in time spent in the box's center and total running distance in the OFT (Fig. 1m, n). Sham controls showed no effects (Fig. 1l, o).

In summary, BLA activation is essential for stress-induced defecation. Defecation bouts, rate, and latency serve as quantifiable, sensitive behavioral measures of stress, reflecting both stress intensity and BLA activation. We define this combination as the "negative emotion index," a set of non-invasive behavioral indicators of stress.

Systemic NVC dysfunction via SMC-specific GluN2D loss exaggerates negative emotion under mild stress

Our previous research identifies a specialized structure within the neurovascular unit (NVU), termed the Neuro-smooth Muscle Junction (NsMJ), where neuronal axon terminals directly contact smooth muscle cells (SMCs) and regulate rCBF via neurotransmitter release (Fig. 2a).[20] We demonstrate that SMC-specific knockout of *Grin1*, the core NMDA receptor subunit, significantly reduces functional hyperemia in the barrel cortex (S1BF) during whisker stimulation.[20] However, the non-core NMDA receptor subunits contributing to receptor formation in SMCs remain unidentified.[21]

To address this, we first examined the expression of all NMDA receptor subunits in brain SMCs. We found that only *Grin2d* (encoding GluN2D) and *Grin1* (encoding GluN1) were detectable (Fig. 2b), a result further confirmed by RNA_{scope} (Fig. 2c; Supplementary information, Fig. S2a, b).[22] We then generated SMC-specific *Grin2d* conditional knockout (*Grin2d-cKO*) mice to

145 assess the role of GluN2D in mediating NVC in both the superficial S1BF and
146 deep BLA (Fig. 2d-k). In *Grin2d-cKO* mice, GluN2D expression was selectively
147 reduced in SMCs, without affecting other brain cell types (Fig. 2d;
148 Supplementary information, Fig. S2c-e).

149 Consistent with our prior findings that *Grin1* deletion impairs NVC, loss of
150 *Grin2d* also disrupted NVC in S1BF during whisker stimulation (Fig. 2e-g). To
151 further explore the impact of *Grin2d* loss on rCBF dynamics in the BLA, we
152 developed a novel paradigm to detect BLA-local NVC in freely moving mice.
153 This approach allowed simultaneous monitoring of BLA rCBV, neuronal Ca^{2+}
154 dynamics, and defecation behavior during the OFT (Fig. 2h).

155 Although regional cerebral blood volume (rCBV) measurements using
156 rhodamine-labeled plasma are well-established in superficial brain regions,
157 their application in deep regions like the BLA required validation.[23] 3D
158 reconstruction revealed abundant arteriole in the BLA, notably the
159 corticoamygdaloid artery (coamg), which originates from the internal carotid
160 artery (Supplementary information, Fig. S3, Video S1), providing structural
161 support for BLA rCBV detection in dilating and contracting arterioles. We
162 confirmed that fiber photometry reliably detected rhodamine fluorescence in the
163 BLA, with a linear signal increase across concentrations from 2.5 to 20 mg/ml
164 (Supplementary information, Fig. S4a, b). For long-term monitoring, we
165 selected a 5 mg/ml concentration, as its signal remained stable for about 900
166 seconds post-injection (Supplementary information, Fig. S4c). All subsequent

167 rCBV recordings were performed under this optimized condition.

168 In control mice, NVC in the BLA exhibited robust functional hyperemia
169 coupled with neuronal activity during OFT exposure (Fig. 2i-k). However,
170 *Grin2d-cKO* mice displayed significantly reduced functional hyperemia, despite
171 elevated neuronal Ca^{2+} signals and c-Fos expression, indicating a decoupling
172 of rCBV from neuronal activity in the BLA (Fig. 2i-k, Supplementary information,
173 Fig. S5). Given the correlation between BLA activity and defecation (Fig. 1d),
174 the heightened BLA neuronal Ca^{2+} and c-Fos might suggest exaggerated
175 negative emotional responses in *Grin2d-cKO* mice. Indeed, these mice
176 exhibited significantly increased defecation bouts during the OFT, especially
177 within the first 5 minutes, reaching 12-fold higher than controls (Fig. 2l).
178 Additionally, the defecation rate increased, and latency was shortened (Fig. 2m;
179 Supplementary information, Table S1).

180 Notably, *Grin2d-cKO* mice also showed a reduction in rearing bouts (Fig.
181 2n), a classic indicator of heightened negative emotional states.[19] Both
182 behavioral changes (defecation, rearing) suggested amplified stress responses
183 in *Grin2d-cKO* mice under mild stress. Importantly, basal rCBV in the BLA,
184 locomotion, area preference, routine food/water consumption, defecation,
185 urination, and intestinal health remained unchanged in *Grin2d-cKO* mice, ruling
186 out confounding factors' impact (Supplementary information, Fig. S6, S7a-n).
187 These basal physiological parameters further confirmed that *Grin2d-cKO* mice
188 were in good general health.

To further probe emotional flexibility in *Grin2d-cKO* mice, we used OFT arenas of varying sizes shown in Fig. 1a to assess *Grin2d-cKO* mice's response to increasing spatial stress intensities (Fig. 2m, o; Supplementary information, Table S1). In control mice, the negative emotion index scaled with stress intensity: as arena size decreased, the negative emotion index shifted (Figs. 1c, 2m, o; Supplementary information, Table S1). In contrast, *Grin2d-cKO* mice exhibited a rigid, exaggerated emotional response: Their defecation bouts peaked immediately upon entering the standard 40 cm OFT and remained unchanged across smaller arena sizes (Fig. 2o). Similarly, defecation rate and latency failed to reflect the spatial stress gradient (Fig. 2m; Supplementary information, Table S1). These findings indicated impaired emotional flexibility, or an emotion rigidity-like state, in NVC-deficient mice.[3, 24]

To exclude non-specific effects, we performed a series of control assays. We verified that SMC contractile proteins (α-SMA and smoothelin) remained unaffected (Supplementary information, Fig. S8) in *Grin2d-cKO* mice. Moreover, GluN2D expression was absent in peripheral vascular SMCs of control mice (Supplementary information, Fig. S9), ruling out systemic side effects of *Grin2d-cKO*. Tamoxifen administration alone had no impact on NVC (Supplementary information, Fig. S10).

In conclusion, GluN2D expression in SMCs was essential for maintaining functional NVC in both BLA and S1BF. Loss of GluN2D in cerebral SMCs impaired NVC, decoupled it from neuronal activity, and triggered exaggerated

211 negative emotional responses under mild stress. These results underscored
212 the importance of normal NVC for maintaining balanced emotional responses.

213

214 **Convergent effects of distinct systemic NVC dysfunction models on**
215 **negative emotional reactivity to mild stress**

216 Relying on a single genetic model of NVC dysfunction can lead to biased
217 conclusions. To address this, we examined a panel of models with selective
218 disruptions in distinct cell types within the NVU (Fig. 2a), targeting both
219 established and previously uncharacterized pathways that mediate NVC, and
220 assessed their impact on stress-induced negative emotional responses.

221 We first generated double cKO of *Grin1* and *Grin2d* in SMCs, which did not
222 exacerbate NVC dysfunction beyond that observed with deletion of either of the
223 genes, functionally confirming that GluN1 and GluN2D likely constitute the
224 NMDA receptor complex in SMCs for NVC regulation (Fig. 3a-c). Furthermore,
225 we generated mice with *Grin2d* deletion across all mural cells, including arterial
226 and venous SMCs and pericytes. Compared to *Grin2d* deletion restricted to
227 arteriolar SMCs (*SMA-CreER* driven), pan-mural cell deletion (*Pdgfrβ-CreER*
228 driven) did not further impair functional hyperemia in the S1BF during whisker
229 stimulation (Fig. 3b, c). Consistent with these results, negative emotion indices
230 were not further altered in double cKO and pan-mural cell-specific *Grin2d-cKO*
231 mice (Fig. 3d, e; Supplementary information, Table S1). To rule out systemic

232 confounds, we confirmed that *Grin2d-cKO* mice did not alter blood-brain barrier
233 (BBB) permeability, which reported to cause NVC-deficiency (Supplementary
234 information, Fig. S7o, p).[25]

235 Next, we disrupted NVC by deleting *Ptgs2* (encoding COX-2) selectively in
236 neurons, as pharmacological inhibition and *Ptgs2* knockout both impair NVC.[20,
237 26-28] Consistently, neuron-specific *Ptgs2-cKO mice* exhibited significantly
238 reduced functional hyperemia in the S1BF and shifted negative emotion indices,
239 closely mirroring the effects of SMC-specific *Grin2d-cKO* (Fig. 3d–h;
240 Supplementary information, Table S1). In contrast, although COX-2 mRNA and
241 protein were detected in SMCs (Supplementary information, Fig. S11), SMC-
242 specific *Ptgs2-cKO* did not affect NVC or emotional responses, highlighting cell-
243 specific mechanisms.

244 Then, we deleted *Acta2* in SMCs, encoding α-SMA, a key contractile
245 protein in SMCs.[29] Surprisingly, only partial reduction of α-SMA was achieved
246 (It may be due to the fact that N-terminal acetylation of actin is irreversible,
247 thereby reducing its degradation efficiency in cells[30-33]), contrasting with the
248 near-complete knockout observed in *Grin2d-cKO* and *Ptgs2-cKO* models (Figs.
249 2d, 3f, and 3i; Supplementary information, Fig. S1c). However, this partial loss
250 was sufficient to induce NVC impairments similar to those observed in other
251 models with near-complete genetic ablation (Fig. 3g, h). Consistently, *Acta2-*
252 *cKO* mice showed exaggerated negative emotional responses, mirroring the
253 phenotypes observed in both *Grin2d-cKO* and *Ptgs2-cKO* (Neuron) models (Fig.

254 3d, e, g, h).

255 Lastly, we also explored the impact of a high-fat diet (HFD) treatment,
256 known to induce NVC dysfunction and emotional dysregulation (Fig. 3j-n).[25, 34]
257 In this independent, clinically relevant model,[35] 4 weeks of HFD feeding
258 increased stress-induced defecation bouts, rate, and shorten defecation
259 latency despite reduced food intake and the absence of BBB disruption (Fig.
260 3d-e; Supplementary information, Fig. S12).[36]

261 The consistent emergence of heightened emotional reactivity across six
262 distinct models of NVC dysfunction—spanning both whole-brain and whole-
263 body manipulations—supports the idea that intact NVC is a necessity and
264 actively modulates emotional states under mild stress.

265

266 **BLA-specific optogenetic NVC suppression amplifies negative emotional**
267 **responses to mild stress**

268 The whole-scale NVC dysfunction models discussed above, which require
269 prolonged induction periods, lack relative spatial and temporal precision in BLA
270 NVC impairment. These NVC dysfunction models limit the ability to specifically
271 assess the necessity of intact NVC in BLA for maintaining emotional
272 homeostasis. To overcome this limitation, we employed optogenetic technology,
273 which allows precise, temporally controlled manipulations, to acutely suppress
274 NVC in the BLA by constricting arterioles.[37]

275 We first generated SMC-specific ChR2-expressing mice (*SMA-*
276 *CreER:Ai32*) and used a fiber-optic setup similar to that in Fig. 2h to locally
277 activate ChR2-expressing SMCs in the BLA while simultaneously monitoring
278 rCBV dynamics (Fig. 4a, b). After optimizing optogenetic protocols in the home
279 cage with minimal stress, we identified a protocol that reliably and reversibly
280 decreased BLA-local rCBV by approximately 3%, with rCBV rapidly returning
281 to baseline after the cessation of stimulation (Fig. 4c, d). This approach enabled
282 precise, reversible control of deep brain arteriole contraction in freely behaving
283 mice.

284 Optogenetic constriction of arterioles in the deep brain attenuated the
285 stress-induced increase in rCBV specifically in the BLA during OFT (Fig. 4e-g).
286 Fourier transform analysis of rCBV dynamics confirmed that OFT stress elicited
287 functional hyperemia in the BLA, which was effectively suppressed by vascular
288 optogenetics (Supplementary information, Fig. S13). This acute manipulation
289 provided a model of localized NVC dysfunction in the BLA, presumably sparing
290 NVC in other brain regions.

291 Notably, this local NVC disruption led to a significant shift in the negative
292 emotion index, notably with an over tenfold increase in the defecation latency
293 (Fig. 4h, i), consistent with the phenotype observed in whole-brain/global NVC
294 manipulation models (Fig. 2, 3). Behavioural analysis also revealed that
295 vascular optogenetics did not affect locomotion anxiety-like states
296 (Supplementary information, Fig. S14a, b). Together, our acute BLA-specific

297 optogenetic model and the chronic whole-brain NVC dysfunction models
298 converge to demonstrate that intact NVC in the BLA was necessary for the
299 proper modulation of negative emotional responses.

300 In addition to blocking stress-induced rCBF increases above baseline that
301 couple with activated BLA during OFT stress, we asked whether transient
302 below-baseline BLA rCBF dynamics—still far from ischemic—could also trigger
303 emotional shifts. In other words, would decoupling basal blood supply from
304 neuronal activity in the BLA lead to an emotional response, even without
305 external stimuli?

306 To investigate this, we conducted the same experimental paradigm with a
307 3% rCBV decrease, but this time in the home cage context (Fig. 4j). $ChR2^+$ mice
308 exhibited sustained rCBV reduction during optogenetic stimulation period (Fig.
309 4j, k). Surprisingly, while home cage conditions typically produced only routine
310 bowel movements (0.23 fecal pellets/15 min), optogenetic activation induced a
311 marked increase in defecation frequency and bouts (2 fecal pellets/15 min; Fig.
312 4l), representing a nearly tenfold elevation and reaching about half the level
313 seen during ARS. Due to limited visibility caused by corncob bedding in the
314 home cage, we quantified total fecal pellet output at the end of testing but were
315 unable to measure defecation latency.

316 Notably, neuronal activity in the BLA was elevated by approximately tenfold
317 (Fig. 4m, n) following the optogenetic rCBV reduction both in the home cage

318 and OFT that did not involve ischemia (hypoxia) in the home cage
319 (Supplementary information, Fig. S14c, d). This heightened BLA activity may
320 explain the increased defecation bouts (Fig. 4l). These results demonstrated
321 that targeted below-baseline rCBV in the BLA alone is sufficient to evoke
322 heightened negative emotional states. The below-baseline rCBV manipulation
323 in the home cage recapitulated the NVC dysfunction seen in *Grin2d-cKO* mice
324 during OFT stress in two respects: BLA hyperactivity and increased defecation
325 (Fig. 2 and 3). This suggested that the mice behave as if experiencing stress,
326 despite being in a low-stress home cage environment.

327 In summary, the convergence of these two lines of loss-of-function
328 evidence, in both OFT and home cage contexts, established that NVC in the
329 BLA is both necessary (in the OFT, Fig. 4e-i) and sufficient (in the home cage,
330 Fig. 4j-l) for the expression of negative emotional states. These findings
331 suggested a direct causal link between BLA NVC and emotional regulation.

332

333 **Whole-brain and BLA-local disruptions of the SMC GluN2D partner**
334 **caldasmon heighten negative emotion under mild stress**

335 To explore the molecular mechanisms by which NVC modulates negative
336 emotions, we focused on GluN2D and its downstream signaling in SMCs. Using
337 co-immunoprecipitation and mass spectrometry, we identified proteins
338 interacting with GluN2D in vascular SMCs. KEGG pathway analysis revealed

339 that caldesmon, an actin-binding protein critical for vascular contraction, was
340 enriched in pathways related to *Vascular Smooth Muscle Contraction* (Fig.
341 5a).[38] Western blotting confirmed the presence of caldesmon in the protein
342 complex immunoprecipitated by anti-GluN2D antibody (Fig. 5b).

343 Caldesmon regulates SMC contractility, and its disruption could impair
344 arteriole dilation, thus affecting NVC.[39] Both mRNA and protein analysis
345 indicated that *Cald*/caldesmon is expressed exclusively by perivascular mural
346 cells,[40] ensuring that siRNA-mediated knockdown (KD) minimally impacts the
347 neuronal circuit directly (Fig. 5c-e). This approach could not be applied to
348 *Grin2d*, as it is also expressed in neurons. Whole-brain *Cald* KD, via CSF
349 delivery of siRNA, attenuated NVC in S1BF during whisker stimulation (Fig. 5f-
350 k), confirming *Cald* KD as an effective strategy for disrupting NVC.

351 BLA-targeted *Cald* KD did not alter caldesmon expression in other regions,
352 such as the nearby VMH (Fig. 5g-i), and functional hemodynamics data
353 confirmed the spatial specificity of this approach (Fig. 5j, k). Behaviorally, global
354 and BLA-targeted *Cald* KD led to BLA neuronal activation and exaggerated
355 negative emotional responses (Fig. 5l-o). This phenotype closely resembled
356 that of *Grin2d-cKO* mice in two ways: BLA hyperactivation (c-Fos expression)
357 and increased defecation behaviors (Fig. 2i-m, 5l-o). Importantly, *Cald* KD in
358 the BLA of *Grin2d-cKO* mice did not further affect the negative emotion index
359 (Fig. 5n, o), suggesting that caldesmon functions downstream of GluN2D in
360 SMCs.

361 Finally, S1BF-restricted *Cald* KD did not affect BLA caldesmon expression
362 and the negative emotion index (Supplementary information, Fig. S15). These
363 findings underscored the region-specific role of BLA NVC in emotional
364 modulation and highlight that proper NVC function in the BLA is particularly
365 critical for modulating negative emotions. Together, our results identify
366 caldesmon as a key effector linking GluN2D to SMC contractility, with BLA NVC
367 impairment was sufficient to promote emotional distress during the OFT.

368

369 **BLA-targeted pharmacological rescue of NVC normalized negative hyper-**
370 **responsiveness to mild stress**

371 To rescue BLA NVC dysfunction in genetic models, we administered HET0016,
372 a cytochrome P450 inhibitor that blocks 20-HETE, a vasoconstrictor.[41, 42] We
373 first confirmed its NVC-enhancing effect through the whisker stimulation assay
374 after global i.p. injection (Fig. 6a). Dose-dependent assays showed that 0.1 and
375 1 mg/kg doses significantly reduced stress-induced defecation bouts in ARS
376 (Supplementary information, Fig. S16a). We adopted 1 mg/kg as the standard
377 dose and confirmed that Het0016 enhanced S1BF hyperemia upon the whisker
378 stimulation (Supplementary information, Fig. S16b, c).

379 In *Grin2d-cKO* mice, both systemic (1 mg/kg, i.p.) and local BLA (10 μM)
380 HET0016 administration normalized excessive negative emotion indices and
381 suppressed rearing bouts (Fig. 6a-f). These results demonstrated that localized

382 pharmacological NVC enhancement can reverse heightened negative
383 emotional responses in whole-brain NVC dysfunction models, underscoring
384 BLA NVC's role in emotional modulation and therapeutic potential. By contrast,
385 HET0016 did not rescue phenotypes in *Acta2-cKO* mice, which directly affects
386 the contract machine of SMCs (Fig. 6g-i), suggesting that SMC contractility is
387 crucial for the observed effects. Moreover, this result indicated that HET0016
388 likely did not act directly on BLA neurons.

389 HET0016 was also tested in HFD mice, where local BLA injection partially
390 restored negative emotion indices (Supplementary information, Fig. S17),
391 although the effect was weaker than in *Grin2d-cKO* mice, likely due to broader
392 brain and vascular alterations. Together, these findings indicated that the
393 HET0016 rescue strategy is effective, but requires responsive arterioles.

394

395 **A topology-based estimation framework of BLA activity for negative**
396 **emotional reactivity to mild and strong stressors**

397 To better classify exaggerated emotional responses caused by NVC
398 dysfunction, we developed an estimation framework based on the link between
399 BLA neuronal activation and stress intensity (Fig. 7). We used seven contexts
400 with increasing stress levels, ranging from minimal stress (home cage) to
401 intense stress (predator-like threat), simulated by the traditional looming
402 assay[43] and a new virtual reality eagle diving task (VR_{eagle}) (Fig. 7a).

403 Contextual mapping revealed a spectrum of BLA activity levels, reflected
404 in c-Fos activation patterns that integrated anatomical distribution and intensity
405 (Fig. 7a). By comparing these patterns across contexts, we created a similarity
406 matrix (Supplementary information, Table S2, See Material and methods).
407 Unsupervised clustering algorithms grouped the seven contexts into four stress
408 levels (0-3), matching expectations: level 0 (home cage), level 1 (OFT), level 2
409 (ARS), and level 3 (Looming, VR VR_{eagle}) (Fig. 7a).

410 Notably, a custom-designed complex OFT—using high-contrast white
411 flooring to heighten stress—was placed between OFT and predator-threat
412 paradigms at level 2 with ARS (Fig. 7a; Supplementary information, Fig.
413 S18a).[44] Looming and VR_{eagle} were both classified as level 3, with VR_{eagle}
414 slightly higher (Fig. 7a; Supplementary information, Fig. S18b, c). This
415 framework proved reliable for estimating stress levels across different contexts.

416 Next, we examined emotional over-responsiveness in NVC dysfunction
417 models (Fig. 7b). NVC dysfunction disrupted c-Fos activation patterns, which
418 were crucial for the estimation framework in normal mice. In the *Grin2d-cKO*
419 mice, the characteristic gradient of BLA c-Fos activity was lost across the seven
420 contexts (Fig. 7b). Only the home-cage context was comparable between
421 genotypes (Fig. 7c), aligning with previous findings of similar basal
422 characteristics (Supplementary information, Fig. S6a).

423 This framework revealed that *Cald* KD and *Grin2d-cKO* mice were the most

similar groups (Fig. 7b, d, e), consistent with caldesmon's role alongside GluN2D (Fig. 5). Despite impaired NVC, both groups exhibited hyper-activation of BLA neurons. Additionally, the framework ranked "cKO_OFT_40" at Level_2, despite these mice experiencing Level_1 stress, indicating hyper-reactivity, which matched observed behaviors (Fig. 2l, m, Fig. 3d, e). Furthermore, arteriole optogenetics caused a two-level increase in stress (from Level_0 to Level_2) (Fig. 7f), indicating that NVC-deficient mice responded excessively to mild stressors.

Unexpectedly, *Grin2d-cKO* mice exhibited diminished responses to the most intense stressors, with their stress level dropping from Level 3 to Level 2 in response to looming and VR_{eagle} paradigms (Fig. 7g, h) (Supplementary information, Fig. S19a). Moreover, while defecation served as a robust index in level 1-2, it failed to distinguish between NVC-impaired and control mice under strong stress (Supplementary information, Fig. S19b, c). This paradoxical hypo-responsiveness under strong stress contrasted with the hyper-reactivity observed under mild stress, highlighting context-dependent, bipolar manifestations of NVC dysfunction. These findings warrant further physiological and behavioral investigation.

NVC dysfunction induces hypo-reactivity: accelerated recovery from strong, virtual predator stress

Innate fear responses to natural predators (e.g., eagles and cats) follow a five-step process: (1) predator detection, (2) threat evaluation, (3) selection of defensive strategy, (4) execution of defense (e.g., fight or flee), and (5) termination of defense and recovery.[45] The fifth step is particularly important: premature termination increases vulnerability, while delayed termination leads to unnecessary energy loss.[45]

Compared to conventional stress paradigms, innate fear assays like Looming and VR_{eagle} are more complex and multidimensional. Due to the limitation of the defecation behavior, to quantify negative emotional responses, we introduced refined behavioral indices—locomotion speed, freezing duration, and pupil diameter—to provide a comprehensive view of emotional dynamics.

We first assessed behavior in the Looming assay, simulating predator approach. When mice reached a speed of 13–15 cm/s, a rapidly expanding black disk was triggered (Supplementary information, Fig. S18b). During baseline (no stimulus), NVC-impaired and control mice showed no difference in locomotion performance (Fig. 8a blue zone; Supplementary information, Fig. S20a), suggesting intact motor function. Upon stimulus, both groups exhibited freezing behavior, reducing speed to 0–2 cm/s (Fig. 8a yellow zone), indicating normal initiation of fear responses (Step 1-4).

Focusing on step 5—termination of defense and recovery—velocity heatmaps showed earlier recovery in NVC-impaired mice (Fig. 8b).

466 Quantitatively, they exhibited significantly faster locomotion speed within 21
467 seconds post-stimulus (Fig. 8c). Additionally, NVC-impaired mice increased
468 rearing bouts after stimulation (Fig. 8d), supporting accelerated recovery. These
469 findings suggested that NVC impairment did not affect the initiation of fear
470 responses but hastens emotional recovery, likely due to lower BLA activation
471 (Fig. 7b; Supplementary information, Fig. S19a).

472 Next, we upgraded the Looming assay to the VR_{eagle} assay to evaluate
473 each stage of fear responses in greater detail. Pupil diameter, a sensitive index,
474 was added to assess the emotional impact of NVC impairment under more
475 ecologically relevant conditions.[46] Mice were head-fixed and allowed to move
476 freely on a float ball (Supplementary information, Fig. S18c), with real-time
477 tracking of locomotion speed and pupil diameter (Supplementary information,
478 Video S2). During the baseline, no significant differences were observed
479 between control and NVC-impaired mice (Supplementary information, Fig.
480 S20b, c).

481 The assay had two stages: (1) eagle call (sound only), and (2) rapid visual
482 dive of an eagle image. In stage (1), both groups exhibited slight freezing, but
483 no significant pupil changes (Fig. 8e blue zone), indicating mild threat
484 perception and intact early-stage processing. In stage (2), both groups showed
485 robust fear responses—freezing and pupil dilation (Fig. 8e yellow zone;
486 Supplementary information, Fig. S20d), confirming normal sensory processing
487 and behavioral execution (steps 1–4).

However, after stimulus termination, we observed significantly faster recovery in NVC-impaired mice. We defined the “defensive offset phase” as the interval between stimulus offset and the point where pupil size line and locomotion speed line in the diagram traces crossed (Fig. 8e brown vertical line to blue/ magenta vertical lines). This phase was markedly shorter in NVC-impaired mice (Fig. 8f). Across both Looming and VR_{eagle} paradigms, the time to baseline recovery (Locomotion speed change for the Looming assay, and pupil size change for the VR_{eagle} assay) was ~12 s in controls, but reduced by ~59% in NVC-impaired mice (Fig. 8g). These results demonstrated a consistent, cross-paradigm reduction in emotional recovery time, potentially linked to lower BLA activation levels.

To assess whether the attenuated negative emotion phenotype is predator-specific, we developed a Cat_{Video} assay presenting a different predatory threat (Supplementary information, Fig. S18d). Head-fixed mice ran on a treadmill while watching a cat stalking and pouncing on prey (Supplementary information, Video S3); retreat behavior and tail rattling were recorded as defensive readouts.

Consistent with previous paradigms, control and NVC-impaired mice did not differ in defecation bouts (Supplementary information, Fig. S19b, c). Control mice exhibited strong defensive behaviors—retreat and tail rattling—indicating threat perception (Fig. 8h-l). In contrast, most NVC-impaired mice showed little or no defensive response, such as significantly reduced retreat behavior and

510 tail rattling (Fig. 8h, j-l).

511 These results confirmed that the diminished innate fear response caused
512 by NVC impairment was not predator-specific but generalized across various
513 aversive contexts. The Cat_{Video} assay, alongside the Looming and VR_{eagle} data,
514 validated that NVC impairment consistently lowers stress levels in strong stress
515 contexts, leading to blunted defense behavior. This highlighted that intact NVC
516 was crucial for calibrating the appropriate emotional intensity and duration
517 during threat exposure, while its disruption elevated the response threshold and
518 shortens defensive states.

519

520 **Evaluation of NVC-dysfunction mice's emotional responsiveness to**
521 **strong, real social aggressor**

522 To extend our findings from virtual paradigms to real-world threats, we designed
523 an aggressive social stress assay to assess how NVC-dysfunction mice
524 respond to actual social stressors. This approach allowed us to evaluate
525 whether NVC-impaired mice exhibit mismatched responses when confronted
526 with real-life stress.

527 C57BL/6 mice, with either intact or impaired NVC, were co-housed with
528 pre-screened aggressive CD1 mice in a new cage divided into small and large
529 compartments by a metal lid (Fig. 9a). The mice were free to move between
530 zones during a 10-minute trial, and social interactions—particularly fighting—

were recorded. As in previous assays, defecation bouts did not differentiate NVC status (Supplementary information, Fig. S19b, c). NVC-normal mice engaged in approximately 20 seconds of fighting (~4% of the session time) (Fig. 9b), which is less than what is typically observed in classic social defeat models where C57BL/6 mice are introduced into the home cage of resident CD1 aggressors.[47] Based on the estimation framework, these mice were classified at stress Level_1 (Fig. 9c).

In contrast, NVC-impaired mice were classified as stress Level_0—equivalent to baseline conditions—even while facing aggressive social stress (Fig. 9d). This indicated emotional hypo-responsiveness. Behavioral analysis confirmed this observation: although both groups avoided sharing the small space with the CD1 aggressor, NVC-impaired mice showed significantly reduced avoidance (Fig. 9e). While 98% of control mice fled during fights, only 37% of NVC-impaired mice actively escaped (Fig. 9f), suggesting an impaired defensive drive. Additionally, NVC-impaired mice experienced fewer attacks (1.9 vs. 4.6 fights per mouse on average) (Fig. 9g). However, both groups exhibited similar levels of sniffing toward the CD1 mice (Fig. 9h), ruling out sensory deficits.

Together, these findings reinforce the crucial role of NVC in generating context-appropriate negative emotional responses. Disruption of NVC resulted in misaligned stress reactivity, weakened defense mechanisms, and blunted emotional responses—highlighting a mechanistic link between cerebrovascular

553 dysfunction and affective disorders.

554

555 **Genetic NVC enhancement prevents strong CRS-induced NVC**
556 **dysfunction and confers resistance to the resulting emotional distress**

557 To further explore the intrinsic genetic regulators that could enhance NVC and
558 mitigate stress-induced emotional dysregulation, we focused on identifying
559 anion channels that might promote NVC. As we had previously shown, NVC
560 impairment was induced by targeting cation channels (NMDA receptors) in
561 SMCs (Fig. 2a). We hypothesized that inhibiting anion channels could enhance
562 NVC and potentially counteract stress-induced negative emotional responses.

563 Through transcriptomic database screening, we identified *Glrb* (encoding
564 GlyRβ), a ligand-gated chloride channel, as being highly expressed in venous
565 SMCs (Supplementary information, Fig. S21).[40] RNA_{scope} and immunostaining
566 further confirmed that GlyRβ was predominantly localized in venous SMCs (Fig.
567 10a–d). To assess its function, we generated *Pdgfrβ-CreER:Glrb*$^{f/f}$ mice to
568 delete *Glrb* specifically in pan-mural cells. GlyRβ expression was significantly
569 reduced in these mice (Fig. 10c, e–f). Additionally, we identified that GlyRβ
570 colocalized with gephyrin *in vitro* (Fig. 10g), a scaffolding protein commonly
571 found in inhibitory postsynaptic sites, suggesting that GlyRβ may cluster on the
572 post-junctional membrane of glycinergic NsMJ. This hypothesis was supported
573 by confocal laser scanning microscopy (Fig. 10h) and electron microscopy (Fig.

574 10i), which showed frequent direct contact of neuronal axons onto venular
575 SMCs.

576 In functional assays, whisker stimulation in *Glrb-cKO* mice led to enhanced
577 functional hyperemia (Fig. 10j, k), indicating potentiated NVC. However, this
578 effect was absent when *Glrb* was deleted specifically in arteriolar SMCs
579 (Supplementary information, Fig. S22a, b), highlighting the crucial role of non-
580 arteriolar mural cells. Behaviorally, NVC-enhanced mice exhibited similar
581 emotional indices to controls under mild stress (OFT) but showed significantly
582 fewer defecation bouts under ARS, suggesting enhanced emotional resilience
583 (Fig. 10m). This effect was absent in SMC-specific *Glrb-cKO* mice
584 (Supplementary information, Fig. S22c).

585 Given that NVC enhancement conferred resilience to stress, we tested
586 whether genetically restoring NVC could reverse the effects of *Grin2d-cKO*. We
587 generated a double cKO model targeting both *Grin2d* and *Glrb* in mural cells
588 (*Pdgfrβ-CreER:Grin2d*$^{f/f}$*:Glrb*$^{f/f}$) to restore the balance between excitatory and
589 inhibitory channels (Fig. 10l). Results confirmed that compared to *Grin2d-cKO*
590 mice, the dual knockouts preserved whisker-stimulation-induced hyperemia
591 (Fig. 10j, k) and normalized emotional indices in the OFT (Fig. 10m, n;
592 Supplementary information, Table S1), indicating that NVC restoration can
593 reverse stress hypersensitivity.

594 To rule out off-target effects of *Glrb* deletion, we used the NVC inhibitor

595 pinacidil, a Kir6.1 activator.[48, 49] Intraperitoneal injection of pinacidil reduced
596 functional hyperemia (Supplementary information, Fig. S23a–c) but also
597 decreased basal cerebral perfusion (Supplementary information, Fig. S23d),
598 suggesting systemic side effects. Global administration of pinacidil abolished
599 ARS-induced defecation in all mice (Supplementary information, Fig. S23e),
600 likely due to effects on SMCs in the cardiac and gastrointestinal systems.[50] To
601 isolate NVC-specific effects, we locally injected pinacidil into the BLA
602 (Supplementary information, Fig. S23a). This intervention abolished the
603 resilience conferred by NVC enhancement, returning defecation bouts to
604 baseline levels (Supplementary information, Fig. S23f), confirming that the
605 resilience originated from local BLA NVC enhancement rather than systemic
606 actions.

607 Finally, we examined whether enhanced NVC could provide long-term
608 resilience to chronic stress, using a chronic restraint stress (CRS) model (Fig.
609 10o).[51, 52] After CRS exposure, control mice exhibited anxiety-like behaviors
610 (reduced open-arm time in the EPM), constipation, and attenuated functional
611 hyperemia (Fig. 10j, k, p, q; Supplementary information, Fig. S24). These
612 effects were absent in NVC-enhanced mice, indicating resistance to CRS (Fig.
613 10j, k, p, q). In the forced swimming test (FST), NVC-enhanced mice exhibited
614 reduced immobility regardless of CRS history (Fig. 10r), consistent with ARS-
615 induced defecation bouts remaining unchanged post-CRS (Supplementary
616 information Fig. S25). These data further confirmed their enhanced emotional

resilience.

Locomotion and anxiety-like assessments excluded locomotor or basal anxiety confounds (Supplementary information, Fig. S26a, b). However, NVC-enhanced mice exhibited weight loss during CRS (Supplementary information, Fig. S26c), suggesting incomplete protection. Since CRS is known to induce BBB disruption and emotional dysfunction, we also evaluated BBB integrity.[53-55] Notably, 28 days of CRS did not induce IgG leakage, suggesting intact BBB integrity (Supplementary information, Fig. S27). These results suggested that enhancing NVC confers protection against both acute and chronic stress.

DISCUSSION

In this study, we demonstrate that bidirectional control of NVC at both systemic and region-specific levels establishes its necessity and sufficiency for modulating negative affect. Thus, NVC exerts causal control over negative-emotion programming, thereby conceptually changing our understanding of NVC. Far from being a passive read-out of neuronal activity, BLA-local NVC operates as an indispensable neurovascular modulator of the BLA network. Disrupting this modulator in the BLA—but not in the primary somatosensory cortex—selectively alters negative emotional outputs, underscoring a region-specific modulation. These findings redefine NVC as an active component of affective circuitry rather than a mere hemodynamic by-product and prompt a re-

638 evaluation of its broader roles throughout the brain.

639 This study introduces a fundamentally independent therapeutic avenue by
640 targeting the mural cell-expressed *Grin2d*, *Cald*, and *Glrb* genes. In particular,
641 *Glrb-cKO* mice has been shown to confer resilience to chronic aversive stress,
642 underscoring the need to develop optimized mural cell–specific delivery
643 systems. Because optogenetically reducing baseline rCBV below in the BLA is
644 sufficient to induce negative emotion (Fig. 4j-n), future pharmacological or
645 neuromodulatory strategies that stabilize or increase this baseline blood flow
646 may offer viable treatments for affective disorders. Collectively, our findings
647 open a new path for intervening in psychopathological progression by
648 enhancing NVC, thus complementing currently existing therapeutic approaches.

649 Our findings demonstrate that baseline hemodynamic states alone can
650 modulate emotion (Fig. 4j-n). This implies hemodynamic or vascular factors as
651 potential initiators of negative affect, aligned with recent causal evidence linking
652 cardiac rate to affective status.[56] This finding also suggest that resting-state
653 fMRI measures of amygdala connectivity reflect not only synaptic interactions
654 but also baseline vascular dynamics, underscoring the need to integrate
655 hemodynamic factors into translational models of affective circuitry.[57]

656 However, a key limitation of this study is that the mechanism by which SMC
657 contraction induced by optogenetics triggers BLA neuronal c-Fos upregulation
658 and negative affect remains unclear. Previous studies have reported that

659 increased hemodynamic flux into penetrating arterioles in the cortical cortex
660 can suppress action potential firing in surrounding neurons, hinting at a
661 potential role for vascular-neuronal coupling (VNC) in mediating these
662 effects.[58-60] This raises the possibility that vascular changes may directly
663 influence neuronal activity through mechanical or metabolic signaling pathways,
664 a hypothesis warranting further investigation to dissect the causal chain linking
665 vascular dynamics to affective states.

666 We developed a refined negative emotion index (bouts, latency, and rate)
667 as a non-invasive and reliable behavioral readout of emotional responses
668 across multiple contexts. Unlike the time-in-center parameter–which only
669 applies to the OFT–this defecation index can be readily applied to diverse
670 behavioral tests. Previous studies have identified a direct monosynaptic circuit
671 between the amygdala and Barrington's nucleus (Bar), a brainstem center that
672 may be implicated in defecation control.[61, 62] Based on this, we hypothesized
673 that optogenetic stimulation of SMCs in the BLA, through yet unknown
674 mechanisms, activates BLA neurons, which then signal to Bar directly or
675 indirectly (Supplementary information, Fig. S28).

676 Importantly, our single integrated platform accomplished all five of the
677 following in the same freely behaving mouse: bidirectional
678 optical/pharmacological control of NVC, simultaneous recording of neuronal
679 activity, concurrent measurement of hemodynamic signals, precise targeting of
680 deep-brain regions (e.g., BLA, Bar), and free behavior monitoring. By

integrating these capabilities into one system, we usher NVC research into a new era–enabling causal, brain region-specific dissections of neurovascular "calculations" underlying affective behavior.

Traditional neuronal computation studies have primarily focused on decoding neuronal electrical activity at the synaptic level, emphasizing how neuronal networks transmit and integrate electrical signals to regulate perception, decision-making, and behavior.[63] We propose that the completeness of neuronal computation could extend beyond synaptic activity and integrate "neurovascular modulatory contribution" to reveal how vascular and hemodynamic changes modulate neuronal circuits in a flexible and fine-tuning manner. The concept of neurovascular computing not only expands our understanding of "computation" in neuroscience but may also offer new biological insights for future artificial intelligence architectures that aim to be able to flexibly and finely tune affective responses.[64]

Negative emotion linked to innate fear is a key survival mechanism. For example, in high-stress situations such as combat or natural disasters, the ability to regulate emotions profoundly influences decision-making and survival outcomes.[45, 65] Our findings show that accelerated recovery from defensive states in the NVC-dysfunction model may increase vulnerability to subsequent threats (Fig.8),[66] offering insight into the evolutionary conservation of NVC across species, as appropriate regulation of innat responses can be a matter of life or death in the animal kingdom and, at times, in human society as well.[67]

703

704 **MATERIALS AND METHODS**

705 **Animal and animal care**

706 All mouse procedures complied with the Institutional Animal Care and Use
707 Committee (IACUC) guidelines of the School of Life Sciences, Westlake
708 University. All mice were housed in the Westlake University Laboratory Animal
709 Resource Centre with standard animal facilities, which provided a 12-hour
710 light/dark cycle at 25 °C. No more than six mice were fed in each cage, and
711 standard chow/water was provided to the mice *ad libitum*. All the genetic
712 information of mice is in Supplementary information, Table S3.

713

714 **Home cage monitor assay**

715 The blood pressure of mice was measured by Kent Noninvasive blood pressure
716 measurement system for animals (Kent/Biopac, USA) before the home cage
717 monitor assay. Each home cage only contains four mice. In each cycle (three
718 days), 60 g of food, 340 g of water (including 100 g bottle weight), and 100 g of
719 padding were provided. Weight of mice, food/water consumption, fecal particles,
720 and urination amount (counted by increased padding weight) were measured
721 by calculating the mean data. Three cycles of monitoring were performed for
722 each home cage. The intestine system inspection was performed after three
723 cycles of monitor. After the assay, mice were fed alone in a clean new cage for

724 90 min and then used for brain extraction to detect c-Fos expression.

725

726 **Open field test**

727 The setup of open field test (OFT) referred to published papers.[14, 19] Each
728 mouse was placed in the central area of a 40*40 cm, 35*35 cm, or 10*10 cm
729 box for the OFT. The camera recording was 15 min. For the chemogenetic
730 manipulation assay, the C21 intraperitoneal injection was 45 min before the
731 OFT. After the assay, mice were fed alone in a clean new cage for 90 min and
732 then used for brain extraction to detect c-Fos expression. For the BLA NVC
733 recording, optic fibers were implanted at BLA (AP: -1.6 mm; ML: +/-3.45 mm;
734 DV: -4.0 mm) with the injection of hSyn-Gcamp-8f virus (*SMA-creER:Ai32* mice
735 do not need virus injection. Detailed information about virus mentioned later)
736 two weeks before the assay. Before the formal assay, three days of adaptation
737 were performed. On the day of the assay, orbital injection of Rhodamine (Sigma,
738 Cat# R9379-1G, USA) 100 μl 5 mg/ml 15 minutes before the recording. 405 nm
739 light was used for bassline control, 473 nm light recording for the Gcamp-8f
740 signal (For *SMA-creER:Ai32* and *SMA-creER:Ai47* mice, using 473 nm light for
741 optogenetic stimulation), and 580 nm light recording for the Rhodamine
742 signal. Recording sustained 15 minutes (For NVC recoding)/45 minutes (For
743 optogenetic stimulation plus rCBV recording). Untouched-rearing bouts
744 measurement in the 1st 5 min. Defecation bouts measurement keep 15 min.

745

746 **Tube stress assay**

747 A 50ml tube was used to restrain the mice to perform acute restraint stress
748 (ARS) and chronic restraint stress (CRS).[54, 68] The tube cover and wall will be
749 drilled to ensure normal breathing. For ARS, the mice were restrained in the
750 tube for 15 min, and then the fecal production was measured. For the ARS plus
751 chemogenetic manipulation assay, the C21 intraperitoneal injection was 45 min
752 before the tube stress assay. After the assay, mice were fed alone in a clean
753 new cage for 90 min and then used for brain extraction to detect c-Fos
754 expression. For CRS, the mice were restrained in the tube for 180 min/day
755 (random time for restraint), constant for 28 days. Fecal production and Bristol
756 Score was measured at the end of each seven days within 60 minutes in a
757 empty home cage box.

758

759 ***In vivo* virus injection**

760 rAAV2/4-Glyt2-EGFP-WPRE-hGHpolyA (5E+12VG/ml) was used to label
761 glycinergic neurons. Two weeks before the assay, bilateral medullary reticular
762 formation injection (500 nl on each side, AP: -3.5 mm; ML: +/-0.84 mm; DV: -
763 2.8 mm)[69] was administered. AAV2/5-mCaMKIIa-hM4D(Gi)-EGFP-ER2-
764 WPRE-pA(2.30E+12VG/ml) and AAV2/5-mCaMKIIa-EGFP-ER2-WPRE-
765 pA(2.30E+12VG/ml) were used for the chemogenetical manipulation. Two

766 weeks before the assay, bilateral amygdala injection (150 nl on each side, AP:
767 -1.6 mm; ML: +/-3.45 mm; DV: -4.1 mm) was administered. AAV2/9-hSyn-
768 jGCaMP8f-WPRE-pA was used for the neuronal calcium measurement. Two
769 weeks before the assay, bilateral amygdala injection (150 nl on each side, AP:
770 -1.6 mm; ML: +/-3.45 mm; DV: -4.1 mm) was administered.

771

772 **Immunofluorescence staining**

773 For Immunofluorescence (IF) staining, after anesthesia with 1% pentobarbital
774 sodium, the mice were perfused with 1X PBS (5 min) and 4% PFA in 1X PBS
775 (5 min) through the left ventricle to empty blood and fix tissue. Afterwards, tissue
776 was extracted and fixed by 4% PFA in 1X PBS for 6 hours at 4 °C. For samples
777 like the brain and peripheral organs, samples were sliced into 50 μm (Leica,
778 Histo-VT1200S, DEU). Then, treated samples with 1% Triton X-100 (Diamond,
779 Cat# A110694-0500, CHN) and 0.25% NDS (Jackson Resources, Cat# 017-
780 000-121, USA) in 1X PBS for 60 min at room temperature. After that, samples
781 were rewashed three times with 1X PBS.

782 In the staining process, the primary antibody diluted with 0.1% Triton X-
783 100 in 1X PBS was used to incubate samples overnight at 4 °C. After the
784 incubation, samples were washed with 1X PBS 10 min (3 replicates). The
785 corresponding secondary fluorescence-conjugated antibody diluted with 0.1%
786 Triton X-100 in 1X PBS was used to incubate samples for 120 min at room

787 temperature. After the incubation, samples were washed with 1X PBS for 10
788 min (3 replicates). After that, 1000X diluted DAPI (Beyotime, Cat# C1002, CHN)
789 was used for nucleus staining. Finally, samples were covered by a glass slice
790 with the mounting medium (SouthernBiotech, 0100-01, USA). Zeiss LSM800
791 (Zeiss, LSM800, DEU) microscopy was used for photography. A list of
792 antibodies is in Supplementary Table S4.

793

794 **RT-PCR**

795 For cultured cells, after obtaining pure sorted $EGFP^+$ cells from the cortex, cells
796 were cultured in 6 cm dishes (Corning, Cat# 430166, USA) with SMCM. After
797 cells reached around 90% density, Trizol (Sangon Biotec, Cat# B511311-0100,
798 CHN) was used for the RNA extraction. For brain tissue, after mice were
799 anesthetized with ice, the cortex or cerebellum of the mice was directly taken
800 out, and TRIzol was used for RNA extraction. After extraction, all RNA samples
801 were reverse transcribed to cDNA (50 ng/μl) using HiScript III 1st Strand cDNA
802 Synthesis Kit (Vazyme, Cat# R312-02, CHN). For the Real-Time Polymerase
803 Chain Reaction (RT-PCR), each reaction contained 10 μl of Green Taq Mix
804 (Vazyme, Cat# P131-AA, CHN), 2 μl of cDNA, 2 μl of primer pairs (10 μM), and
805 6 μl of RNAase-free water. Agarose gel electrophoresis used 2 % agarose gel
806 (BIOWESTE, Cat# 111860, ESP) and ran at 220 V for 30 min. RT-PCR gel
807 images were obtained from a Tanon imager (Tanon, 1600 Geil imager, CHN). A

808 list of primer pairs is in Supplementary Table S5.

809

810 **RNA$_{scope}$ in situ hybridisation**

811 Horizontal sections (15 μm) of tamoxifen administrated *SMA-creER:Ai14* (for
812 *Grin2d*), *Pdgfrβ-creER:Ai14* (for *Glrb*) and C57/B6 *wild-type* (for *Grin2d* and
813 *Grin1* probe validation) mice brains were obtained by CM1950 (Lecia, Histo-
814 CM1950, DEU). All RNA scope *in situ* hybridisation productions were obtained
815 from ACDbio, including RNA$_{scope}$ Multiplex Fluorescent Reagent Kit v2 (ACDbio,
816 Cat# 323100, USA), *Grin2d* probe (ACDbio, Cat# 425951-C3, USA), *Grin1*
817 probe (ACDbio, Cat# 431611, USA), and *Glrb* probe (ACDbio, Cat# 1225261-
818 C1, USA). All operations were carried out following the reagent instructions of
819 ACDbio company and the published paper.[20, 70]

820

821 **siRNA cisternal magna/BLA local injection**

822 Cisterna magna injection protocol referred to Cannula Implantation into the
823 cisterna magna of Rodents (https://doi.org/10.3791/57378) and paper
824 published by our laboratory.[20] 1 nM siRNA was mixed with FITC (10 mg/ml,
825 Sigma, FD40S-1G, USA) for injection (20 μl in total). The scalp was opened 10
826 min after the injection, and the microscope was used to detect the FITC signal
827 (Zeiss, Axio Zoom v16, DEU) in perivascular spaces. Only successfully injected
828 mice remain. Whisker stimulation was performed 48 hours after siRNA injection,

829 followed by 40 cm OFT. As for BLA local siRNA injection, 150nl of 1nM siRNA
830 was injected in two sides of BLA (AP: -1.55 mm; ML: +/-3.40 mm; DV: -4.00
831 mm), and 40 cm OFT was performed 48 hours after siRNA injection. Brain slice
832 collection was performed 90 minutes after OFT for IF staining. Sequence of
833 siRNA can be found in the Supplementary information, Table S5.

834

835 **Cell culture**

836 *SMA-creER:Ai47* Post-born 0-day (P0) mice were anesthetized with ice.
837 Surgical tweezers were used to quickly extract the cortex and then transfer it
838 into the 0.25% Trypsin (Thermo Scientific, Cat# 25200072, USA) for 15 min at
839 37 °C. Next, FBS (Gibico, Cat# 10099, USA) was added to block digestion.
840 Then, cells were filted by a 40 μm filter (Falcon, Cat# 352340, CHN). Finally,
841 cells were centrifuged 1,600*g at 4 °C for 5 min and resuspended by SMCM
842 (ScienCell, Cat# 1101, USA) in T25 flasks (Corning, Cat# 430639, USA). When
843 cells reached approximately 80% full of the bottom surface of T25 flasks,
844 tamoxifen was administrated to cells. Tamoxifen was dissolved in DMSO
845 (Solarbio, Cat# D8371, CHN), and the final concentration of tamoxifen was 5
846 μM. After a four-day culture, EGFP in cells were expressed. Cells were sorted
847 by MA-900 (Sony, FCCF-MBR, JPN) to obtain $EGFP^+$ cells. Sorted cells were
848 cultured in SMCM for further assay. The purity of cells sorted by the same
849 method was verified in a paper published by our laboratory.[71] For data in Fig.

850 10f, samples were directly sorted from Pdgfrβ$^+$ cells in brain lysis by using Anti-
851 Pdgfrβ antibody (without cell culture). Then, Pdgfrβ$^+$ cells were quickly
852 resuspended by Trizol for RNA extraction. A list of antibodies is in Table S44. In
853 Fig. 10g, Human Umbilical Vein Smooth Muscle Cells (HU-vSMC, Sciencell,
854 Cat# 8020, USA) were used for cell culture.

855

856 **Tamoxifen and drug administration for mice**

857 Tamoxifen (MCE, Cat# HY-13757A, USA) was dissolved in corn oil (Aladdin,
858 Cat# C116023-500ml, CHN) and orally administered to mice (10 mg/ml, 200 μl
859 per mouse per day). For *Acta2* cKO, tamoxifen was given from P21 to P24.
860 Otherwise, tamoxifen was orally administered to mice from P60 to P63.

861 For drug delivery, intraperitoneal injection was used for global
862 administration. The total volume is 200 μl. For local administration into the BLA
863 (AP: -1.6 mm; ML: +/-3.45 mm; DV: -4.0 mm), a cannula drug delivery system
864 (RWD, Cat# 800-00245-00, CHN) was employed. The concentrations used for
865 local delivery were 10 μM for Het0016 and 50 μM for pinacidil. The total delivery
866 volume was 1 μl (at a rate of 250 nl/min), and behavioral assays were
867 conducted 5 minutes after Het0016 administration or 25 minutes after pinacidil
868 administration.

869

870

871 **Western-blot**

872 For tissue sample collection, samples were ground with RIPA (Thermo
873 Scientific, Cat# 89901, USA) in the tube on ice for 30 min. For cells, after they
874 reached around 90% density, the RIPA was used for protein extraction on ice
875 for 30 min. Protease Inhibitor Cocktail (CWBIO, Cat# CW22008, CHN) was
876 added into RIPA to prevent protease. After that, samples were centrifuged at
877 12,000*g at 4 °C for 5 min, and the supernatant was collected. Concentrations
878 of proteins were measured by Micro BCA Protein Assay kit (CWBIO, Cat#
879 CW2011S, CHN), and all samples were boiled with SDS-PAGE loading buffer
880 (CWBIO, Cat# CW0027S, CHN) for 10 min at 100 °C. 8% SDS-polyacrylamide
881 electrophoresis gels were used for gel running. After 90 min, gels running at
882 120 V (80 V for the first 30 min), gels were transferred to 0.45 μm PVDF
883 membranes (Millipore, Cat# IPVH00010, USA) at 400 mA for 120 min. After
884 transfer, PVDF membranes were blocked by 5% non-fat milk in 1X TBST buffer
885 for 60 min at room temperature with a mild horizontal shake.

886 After the block, the primary antibody diluted with 5% non-fat milk in 1X
887 TBST buffer was used to incubate the membrane overnight at 4 °C with a mild
888 horizontal shake. After the incubation, the membrane was washed by 1X TBST
889 10min (3 replicates). The corresponding secondary HRP-conjugated antibody
890 diluted with 5% non-fat milk in 1X TBST buffer was used to incubate the
891 membrane for 45 minutes at room temperature with a mild horizontal shake.
892 After the incubation, the membrane was washed with 1X TBST for 10 min (3

893 replicates). ECL kits (Abbkine, Cat# BMU102-CN, CHN) and gel image system
894 (GE, GEL Imaging System AI680RGB v.2.0, USA) were used for exposure
895 photography. A list of antibodies is in Supplementary information, Table S4.

896

897 **Whisker stimulation**

898 Mice were anaesthesia with 1% pentobarbital sodium and open the scalp, then
899 mice stable fixated on the holder. The electro-motor-driven brush stimulated the
900 whisker longitudinally for 1 minute at a frequency of 12 Hz. The principle of laser
901 speckle contrast imaging has been described in the previous paper, and the
902 operation referred to in the published paper.[20, 23, 72] Laser Speckle Image
903 System (RWD, RFSLI ZW/RFSLI III, CHN) was used to record the CBF change
904 in the ROI of the opposite barrel cortex of mice. The recording parameters were
905 512*512 resolution, 10 FPS, and 2-minute recording.

906

907 **Home cage optogenetic stimulation and recording**

908 Optogenetic stimulation referred published papers.[37, 73, 74] *SMA-creER:Ai32*
909 and *SMA-creER:Ai47* mice were used for optogenetic stimulation. Tamoxifen
910 was administered to mice 18 days before tha assay. Then, optic fibers were
911 implanted at BLA (AP: -1.6 mm; ML: +/-3.45 mm; DV: -4.0 mm) two weeks
912 before the assay. Before the formal assay, three days of adaptation were
913 performed. On the day of the assay, orbital injection of Rhodamine 100 μl 5

914 mg/ml 15 minutes before the recording. 405 nm light was used for bassline
915 control, 580 nm light recording for Rhodamine signal for 45 min, and 473 nm
916 light for optogenetic stimulation was performed at the 2nd 15 min of the 45 min
917 recording. The parameters of the stimulation protocol included the stimulation
918 period, interval period, recording period, total frequency, and laser power. The
919 optimal protocol shown in Fig. 4c is 85 ms stimulation, 5 ms interval, 5 ms
920 recording, 10 Hz frequency, 0.939 mW laser power. During the 45-minute
921 recording, mice always stayed in their home cage, but all fecal particles were
922 removed before the assay. After 45 min recording, fecal particles were recorded.

923

924 **Tissue transparency**

925 Mouse brain tissues were washed three times with 1×PBS at room temperature,
926 each lasting two hours, and were processed on a shaker at 40 rpm.
927 Subsequently, a commercial tissue clearing kit (Nuohai, Cat# NH-CR-210701,
928 CHN) was used to perform the clearing procedure according to the
929 manufacturer's standard protocol. The cleared tissues were subjected to three-
930 dimensional imaging using a light-sheet fluorescence microscope (Nuohai,
931 Cat# LS18, CHN) with a laser wavelength of 561 nm. After imaging, the
932 acquired data were preliminarily processed using LS18 image stitching
933 software to generate complete three-dimensional image datasets. The datasets
934 were then imported into ImageJ software for downsampling, with a

935 downsampling factor of 0.25 in the x, y, and z directions. The downsampled
936 datasets were converted into coronal section stacks using the reslice function
937 in ImageJ. The converted datasets were further imported into the BIRDS plugin
938 and registered against the whole-brain atlas (Allen Mouse Brain Common
939 Coordinate Framework version 3, CCFv3). After registration, Imaris Surface
940 modules corresponding to different brain regions were created based on the
941 registration results. Using the Surface modules of each brain region, the
942 acquired three-dimensional data were segmented, and the Surface modules of
943 vasculature for each brain region were generated based on the fluorescent
944 signals. Finally, vascular volume data were obtained by analyzing the volumes
945 of arterial vessels and vasculature in each brain region.

946

947 **Immunoprecipitation assay**

948 tdTomato^{+} sorted aSMCs from P0 *SMA-creER:Ai14* mice were used for
949 lentivirus infection and further immunoprecipitation (IP) assay. Sorted cells were
950 cultured in 6 cm dishes with SMCM. After cells reach around 90% density, add
951 lentivirus (Lenti-EF1-EGFP-CMV-grin2d-3XFlag-WPRE) into the culture and
952 keep for one week to over-express GluN2D. MA-900 sorted out EGFP and
953 tdTomato double-positive cells, which were lentivirus-infected aSMCs. These
954 cells were then cultured in 10 cm dishes. After cells reached around 90%
955 density, cells were collected by RIPA reagent. The Protein G Magnetic beads

956 kit (Epizyme, Cat# YJ002, CHN) was used for the immunoprecipitation assay.
957 GluN2D and IgG control antibodies were mixed with Protein G Magnetic beads
958 to pull down GluN2D and its related protein. Pull-down products were verified
959 by Western-blot and analyzed through mass spectrometry. A list of antibodies
960 is in Supplementary information, Table S5.

961

962 **High-fat diet challenge assay**

963 Set up of High-fat diet (HFD) challenge referred to published papers.[25, 34, 36]
964 Normal fat die (NFD) mice used as control. Mice were given high-fat food
965 (SYSE, Cat# PD6001, CHN) for four weeks. The weight of mice and food
966 consumption were measured before the assay and at the end of each week.
967 The home cage fecal production was measured using the same method
968 mentioned in the *home cage monitor assay* part. 40 cm OFT assay and whisker
969 stimulation assay were performed after four weeks of HFD challenge.

970

971 **BBB leakage inspection (evens blue and IgG)**

972 Assay setup referred to published papers.[36, 75] 2% evens blue (Merck,
973 Cat#E2129, USA) dissolved in saline was used for orbital injection (4 ul/g). After
974 45 min, the mouse was anesthetized, and the brain was extracted for
975 appearance inspection for BBB leakage using a microscope (Zeiss, Axio Zoom
976 v16, DEU). The brain was weighted and then homogenized using 1 ml of 50%

977 trichloroacetic acid (Merck, Cat#190780, USA). Then, samples were
978 centrifuged at 10,000*g at 4 °C for 20 min, supernatants were collected, and
979 absorbance detection at 620 nm was performed. For IgG inspection methods,
980 see the *Immunofluorescence staining* part above.

981

982 **Colorectal inspection**

983 The ENDOQ Colonoscopy system took representative images of colorectal
984 tissue. A professional physician performed scoring of the endoscopic images in
985 a double-blind manner to ensure unbiased assessment.

986

987 **Hematoxylin and eosin staining**

988 For hematoxylin and eosin (HE) staining, after anesthesia with 1% pentobarbital
989 sodium, the mice were perfused with 1X PBS (5 min) and 4% PFA in 1X PBS
990 (5 min) through the left ventricle to empty blood and fix tissue. Afterward, tissue
991 was extracted and fixed by 4% PFA in 1X PBS for 6 hours at 4 °C. After a
992 paraffin block, tissues were sliced into 8 μm sections and examined following
993 HE staining.

994

995 **Topology-based estimation framework**

996 The topology-based estimation framework is based on the Structural Similarity

Index (SSIM) and the cluster analysis of SSIM (See *Statistical analysis software and code* part for details). In brief, translating BLA's c-Fos positive cells location and density with different contexts into SSIM. Then, the cluster analysis was used to classify the SSIM of different contexts to build a library of topology-based estimation framework. To predict a subject's “real” stress level, the SSIM of this subject will be clustered together with the topology-based estimation framework library to locate the subject's stress level.

Complex-Open field test

The complex-open field test (complex OFT) setup referred to a published paper.[44, 76] Each mouse was placed in the central area of the left part of the complex OFT box. One side of the complex OFT box has a white bottom (the mouse is put on this side) and a black bottom on the other. The camera recording was 20 min. After the assay, mice were fed alone in a clean new cage for 90 minutes and then used for brain extraction to detect c-Fos expression.

Looming assay

The assay was carried out in a 35 cm*35 cm OFT box. The settings of the assay were based on the published paper.[43] Modifications include: Modifications include:

- mice will be put in the OFT box to adapt for 10 minutes before starting the assay;
- we only use a single camera at the top of the box to record;
- we stimulate the mice when they move and are not close to the box wall rather than continuously stimulating them.

Each mouse performs one trial of stimulation. After the assay, mice were fed alone in a clean new cage for 90 min and then used for brain extraction to detect c-Fos expression.

VR_{eagle} assay

Assay set up referred published paper.[43] The mouse head was fixed with a fixator two weeks before the assay. The mice received daily adaptive training on the VR system one week before the assay. On the day of the assay, the mice were fixed on the VR system and given 5 min of adaptation. Unless stimulated, the screen in front of the mouse will always play the regular landscape video. The stimulation of the eagle lasts for three seconds. The eagle dives down from far to near and plays the voice of the eagle at the beginning of the stimulation. The criterion for the stimulation was that the mice moved for the first time after 5 min of adaptation. The assay ended 2 min after the stimulation. The pupil changes and mice's locomotion speed were recorded simultaneously. After the assay, mice were fed alone in a clean new cage for 90 min and then used for

1038 brain extraction to detect c-Fos expression.

1039

1040 **Cat_{video} stimulation assay**

1041 The assay was carried out in a 40*40 cm OFT box. The mouse head was fixed
1042 with a fixator and trained to fit the treadmill two weeks before the assay. On the
1043 day of the assay, the mice were anesthetized with isoflurane and fixed on the
1044 treadmill. After the mouse wakes up, play the video of cat hunting on the iPad
1045 Air (Apple. Cat# 3rd generation, USA) in front of the mouse. A camera directly
1046 above was used to record the assay.

1047

1048 **Aggressive social stress assay**

1049 The setup of the home cage social assay referred to published papers.[47, 76-79]
1050 Selected aggressive CD1 mice never exposed to *Grin2d*$^{f/f}$ or *SMA-*
1051 *creER:Grin2d*$^{f/f}$ mice were used for the assay. Before the assay, simultaneously
1052 put a single *Grin2d*$^{f/f}$ or *SMA-creER:Grin2d*$^{f/f}$ mouse and a CD1 mouse into a
1053 cage. The cage contains new padding and a metal lid on the top. One side of
1054 the metal lid is used to place food and water bottles, so the height is lower than
1055 the other. A camera was used to record two mice's behaviours for 10 min. After
1056 the assay, the mice were separated again. *Grin2d*$^{f/f}$ or *SMA-creER:Grin2d*$^{f/f}$
1057 mice were fed alone in a clean new cage for 90 min and then used for brain
1058 extraction to detect c-Fos expression.

1059

1060 **Serial block-face scanning electron microscopy image**

1061 The specimen was obtained in the same batch as the previously published
1062 paper from our laboratory. The details in the *SBF-SEM imaging* part of the
1063 methods in that paper. In brief, the ascending venule was identified using X-ray
1064 microscopy (Zeiss, XRM, Xradia 520 Versa, DEU) at ×4 and 80 kV
1065 magnification. The specimen adhered to an aluminium metal pin using
1066 conductive epoxy (Chemtronics, CW2400, USA). Then, it was further precisely
1067 trimmed into a block of 600*600*700 μm^3 using a glass knife and a right-angled
1068 diamond knife (DiATOME, Trim 90, CHE) after coating with gold-palladium
1069 (Leica, EM ACE200, DEU) and a final trim using a 3View ultramicrotome (Gatan,
1070 USA). Image acquisition was performed using a BSE detector on a Carl Zeiss
1071 Gemini 300 scanning electron microscope at 2 kV voltage and approximately
1072 1.8*10−3 mBar in high-vacuum mode with focus charge compensation. The
1073 specimens were sectioned at a 50–75 nm thickness and a cutting speed of 0.1
1074 mm/s.

1075

1076 **Elevated plus-maze test**

1077 The setup of elevated plus-maze (EPM) referred to published papers.[70, 80] The
1078 EPM comprises two open arms (65 cm * 5 cm) and two close arms (65 cm * 5
1079 cm). Each mouse was placed in the centre, facing one of the two open arms,

1080 and allowed to explore for 5 min. Time spent in open arms was recorded.

1081

1082 **Force Swimming Test**

1083 The Force Swimming Test (FST) referred to a published paper.[81] In brief, mice
1084 were put into the glass water tank with 25 °C clear water. Measuring the
1085 swimming time of mice in 5 minutes and then putting the mouse back in the
1086 home cage.

1087

1088 **Statistical analysis software and code**

1089 All the image processing and analysis of fluorescence intensity used Zeiss Zen
1090 Lite (v3.4) and ImageJ (v1.53u). All whisker stimulation original data were
1091 measured by RWD LSIS-self software (v5.0). All the original behavioral data for
1092 OFT/complex OFT/EPM were recorded using Noldus. Data recording and
1093 analysis of Looming and VR_{eagle} assay was performed using self-compiled
1094 codes provided by Bayonne company. All statistical data were processed by
1095 Numbers (v12.2). All figures were made by Prism (v9.4.1) and Adobe Illustrator
1096 2024 (v28.3). CBF peak mean value, heat maps, mass spectrometry data
1097 inclusion criteria, cross-correlation, and prediction index (based on the
1098 Structural Similarity Index, SSIM) were analyzed by self-compiled MATLAB
1099 codes. Besides, the KEGG pathways, and cluster analysis of SSIM were using
1100 self-compiled R code. All available codes can be found at

https://github.com/JialabEleven/Functional_hyperemia_regulates_emotion.

REFERENCES

1 Roelofs K, Bramson B, Toni I. A neurocognitive theory of flexible emotion control: The role of the lateral frontal pole in emotion regulation. *Ann N Y Acad Sci* 2023; **1525**:28-40.

2 Bortolon C, Chen S, Bonanno GA. Components of emotion regulation flexibility and psychosis: The association between psychosis-proneness and context sensitivity. *Br J Clin Psychol* 2023; **62**:82-95.

3 D'Agostino A, Covanti S, Rossi Monti M, Starcevic V. Reconsidering Emotion Dysregulation. *Psychiatr Q* 2017; **88**:807-825.

4 Easdale-Cheele T, Parlatini V, Cortese S, Bellato A. A Narrative Review of the Efficacy of Interventions for Emotional Dysregulation, and Underlying Bio-Psycho-Social Factors. *Brain Sci* 2024; **14**.

5 De Prisco M, Oliva V, Fico G *et al.* Emotion dysregulation in bipolar disorder compared to other mental illnesses: a systematic review and meta-analysis. *Psychol Med* 2023; **53**:7484-7503.

6 Geng H, Xu P, Aleman A, Qin S, Luo YJ. Dynamic Organization of Large-scale Functional Brain Networks Supports Interactions Between Emotion and Executive Control. *Neurosci Bull* 2024; **40**:981-991.

7 Szaflarski JP, Allendorfer JB, Heyse H, Mendoza L, Szaflarski BA, Cohen N. Functional MRI of facial emotion processing in left temporal lobe epilepsy.

1123 *Epilepsy Behav* 2014; **32**:92-99.

1124 8 Etkin A, Wager TD. Functional neuroimaging of anxiety: a meta-analysis of
1125 emotional processing in PTSD, social anxiety disorder, and specific phobia. *Am*
1126 *J Psychiatry* 2007; **164**:1476-1488.

1127 9 Mathias EJ, Kenny A, Plank MJ, David T. Integrated models of neurovascular
1128 coupling and BOLD signals: Responses for varying neural activations.
1129 *Neuroimage* 2018; **174**:69-86.

1130 10 Iadecola C. The Neurovascular Unit Coming of Age: A Journey through
1131 Neurovascular Coupling in Health and Disease. *Neuron* 2017; **96**:17-42.

1132 11 Pico-Perez M, Radua J, Steward T, Menchon JM, Soriano-Mas C. Emotion
1133 regulation in mood and anxiety disorders: A meta-analysis of fMRI cognitive
1134 reappraisal studies. *Prog Neuropsychopharmacol Biol Psychiatry* 2017; **79**:96-
1135 104.

1136 12 Shen J, Wang D, Wang X *et al.* Neurovascular Coupling in the Dentate Gyrus
1137 Regulates Adult Hippocampal Neurogenesis. *Neuron* 2019; **103**:878-890 e873.

1138 13 Phillips ML, Drevets WC, Rauch SL, Lane R. Neurobiology of emotion
1139 perception II: Implications for major psychiatric disorders. *Biol Psychiatry* 2003;
1140 **54**:515-528.

1141 14 Hale MW, Hay-Schmidt A, Mikkelsen JD, Poulsen B, Shekhar A, Lowry CA.
1142 Exposure to an open-field arena increases c-Fos expression in a distributed
1143 anxiety-related system projecting to the basolateral amygdaloid complex.
1144 *Neuroscience* 2008; **155**:659-672.

1145 15 Kovacs LA, Schiessl JA, Nafz AE, Csernus V, Gaszner B. Both Basal and
1146 Acute Restraint Stress-Induced c-Fos Expression Is Influenced by Age in the
1147 Extended Amygdala and Brainstem Stress Centers in Male Rats. *Front Aging*
1148 *Neurosci* 2018; **10**:248.
1149 16 Kakol-Palm D, Brusberg M, Sand E *et al.* Role of tachykinin NK(1) and NK(2)
1150 receptors in colonic sensitivity and stress-induced defecation in gerbils. *Eur J*
1151 *Pharmacol* 2008; **582**:123-131.
1152 17 Taguchi R, Shikata K, Furuya Y *et al.* Selective corticotropin-releasing factor
1153 1 receptor antagonist E2508 reduces restraint stress-induced defecation and
1154 visceral pain in rat models. *Psychoneuroendocrinology* 2017; **75**:110-115.
1155 18 Monarca RI, Silva RFB, Gabriel SI, Cerveira AM, von Merten S. The
1156 Presence of a Shelter in an Open Field Test Has Differential Effects on the
1157 Behavior and Stress Response of Two Mouse Species. *J Exp Zool A Ecol Integr*
1158 *Physiol* 2025; **343**:480-492.
1159 19 Sturman O, Germain PL, Bohacek J. Exploratory rearing: a context- and
1160 stress-sensitive behavior recorded in the open-field test. *Stress* 2018; **21**:443-
1161 452.
1162 20 Zhang D, Ruan J, Peng S *et al.* Synaptic-like transmission between neural
1163 axons and arteriolar smooth muscle cells drives cerebral neurovascular
1164 coupling. *Nat Neurosci* 2024; **27**:232-248.
1165 21 Laurie DJ, Bartke I, Schoepfer R, Naujoks K, Seeburg PH. Regional,
1166 developmental and interspecies expression of the four NMDAR2 subunits,

1167 examined using monoclonal antibodies. *Brain Res Mol Brain Res* 1997; **51**:23-
1168 32.
1169 22 Monyer H, Burnashev N, Laurie DJ, Sakmann B, Seeburg PH.
1170 Developmental and regional expression in the rat brain and functional
1171 properties of four NMDA receptors. *Neuron* 1994; **12**:529-540.
1172 23 Li J, Zhang Y, Zhang D *et al.* Ca(2+) oscillation in vascular smooth muscle
1173 cells control myogenic spontaneous vasomotion and counteract post-ischemic
1174 no-reflow. *Commun Biol* 2024; **7**:332.
1175 24 Thompson RA. Methods and measures in developmental emotions research:
1176 some assembly required. *J Exp Child Psychol* 2011; **110**:275-285.
1177 25 Huber G, Ogrodnik M, Wenzel J *et al.* Telmisartan prevents high-fat diet-
1178 induced neurovascular impairments and reduces anxiety-like behavior. *J Cereb*
1179 *Blood Flow Metab* 2021; **41**:2356-2369.
1180 26 Lecrux C, Toussay X, Kocharyan A *et al.* Pyramidal neurons are "neurogenic
1181 hubs" in the neurovascular coupling response to whisker stimulation. *J*
1182 *Neurosci* 2011; **31**:9836-9847.
1183 27 Lacroix A, Toussay X, Anenberg E *et al.* COX-2-Derived Prostaglandin E2
1184 Produced by Pyramidal Neurons Contributes to Neurovascular Coupling in the
1185 Rodent Cerebral Cortex. *J Neurosci* 2015; **35**:11791-11810.
1186 28 Niwa K, Araki E, Morham SG, Ross ME, Iadecola C. Cyclooxygenase-2
1187 contributes to functional hyperemia in whisker-barrel cortex. *J Neurosci* 2000;
1188 **20**:763-770.

1189 29 Hill RA, Tong L, Yuan P, Murikinati S, Gupta S, Grutzendler J. Regional Blood
1190 Flow in the Normal and Ischemic Brain Is Controlled by Arteriolar Smooth
1191 Muscle Cell Contractility and Not by Capillary Pericytes. *Neuron* 2015; **87**:95-
1192 110.
1193 30 Heissler SM, Chinthalapudi K. Structural and functional mechanisms of actin
1194 isoforms. *FEBS J* 2025; **292**:468-482.
1195 31 Mayer A, Siegel NR, Schwartz AL, Ciechanover A. Degradation of proteins
1196 with acetylated amino termini by the ubiquitin system. *Science* 1989; **244**:1480-
1197 1483.
1198 32 Ree R, Varland S, Arnesen T. Spotlight on protein N-terminal acetylation.
1199 *Exp Mol Med* 2018; **50**:1-13.
1200 33 Kashina AS. Regulation of actin isoforms in cellular and developmental
1201 processes. *Semin Cell Dev Biol* 2020; **102**:113-121.
1202 34 Li W, Prakash R, Chawla D *et al.* Early effects of high-fat diet on
1203 neurovascular function and focal ischemic brain injury. *Am J Physiol Regul*
1204 *Integr Comp Physiol* 2013; **304**:R1001-1008.
1205 35 Yang S, Webb AJS. Reduced neurovascular coupling is associated with
1206 increased cardiovascular risk without established cerebrovascular disease: A
1207 cross-sectional analysis in UK biobank. *J Cereb Blood Flow Metab*
1208 2024:271678x241302172.
1209 36 Chang HC, Tai YT, Cherng YG *et al.* Resveratrol attenuates high-fat diet-
1210 induced disruption of the blood-brain barrier and protects brain neurons from

1211 apoptotic insults. *J Agric Food Chem* 2014; **62**:3466-3475.

1212 37 Hauglund NL, Andersen M, Tokarska K *et al.* Norepinephrine-mediated slow
1213 vasomotion drives glymphatic clearance during sleep. *Cell* 2025; **188**:606-622
1214 e617.

1215 38 Foster DB, Shen LH, Kelly J, Thibault P, Van Eyk JE, Mak AS.
1216 Phosphorylation of caldesmon by p21-activated kinase. Implications for the
1217 Ca(2+) sensitivity of smooth muscle contraction. *J Biol Chem* 2000; **275**:1959-
1218 1965.

1219 39 Yao YB, Xiao CF, Lu JG, Wang C. Caldesmon: Biochemical and Clinical
1220 Implications in Cancer. *Front Cell Dev Biol* 2021; **9**:634759.

1221 40 Vanlandewijck M, He L, Mae MA *et al.* A molecular atlas of cell types and
1222 zonation in the brain vasculature. *Nature* 2018; **554**:475-480.

1223 41 Liu X, Li C, Falck JR, Roman RJ, Harder DR, Koehler RC. Interaction of
1224 nitric oxide, 20-HETE, and EETs during functional hyperemia in whisker barrel
1225 cortex. *Am J Physiol Heart Circ Physiol* 2008; **295**:H619-631.

1226 42 Renic M, Klaus JA, Omura T *et al.* Effect of 20-HETE inhibition on infarct
1227 volume and cerebral blood flow after transient middle cerebral artery occlusion.
1228 *J Cereb Blood Flow Metab* 2009; **29**:629-639.

1229 43 Shang C, Chen Z, Liu A *et al.* Divergent midbrain circuits orchestrate escape
1230 and freezing responses to looming stimuli in mice. *Nat Commun* 2018; **9**:1232.

1231 44 Shoji H, Miyakawa T. Effects of test experience, closed-arm wall color, and
1232 illumination level on behavior and plasma corticosterone response in an

1233 elevated plus maze in male C57BL/6J mice: a challenge against conventional
1234 interpretation of the test. *Mol Brain* 2021; **14**:34.
1235 45 Silva BA, Gross CT, Graff J. The neural circuits of innate fear: detection,
1236 integration, action, and memorization. *Learn Mem* 2016; **23**:544-555.
1237 46 Wang L, Chen IZ, Lin D. Collateral pathways from the ventromedial
1238 hypothalamus mediate defensive behaviors. *Neuron* 2015; **85**:1344-1358.
1239 47 Bigi S, Maestripieri D, Aloe L, Alleva E. NGF decreases isolation-induced
1240 aggressive behavior, while increasing adrenal volume, in adult male mice.
1241 *Physiol Behav* 1992; **51**:337-343.
1242 48 Zhou H, Neudecker V, Perez-Zoghbi JF, Brambrink AM, Yang G. Age-
1243 dependent cerebral vasodilation induced by volatile anesthetics is mediated by
1244 NG2(+) vascular mural cells. *Commun Biol* 2024; **7**:1519.
1245 49 Bowen RM, York NW, Padawer-Curry J, Bauer AQ, Lee JM, Nichols CG.
1246 Control of neurovascular coupling by ATP-sensitive potassium channels. *J*
1247 *Cereb Blood Flow Metab* 2025; **45**:1130-1143.
1248 50 York NW, Parker H, Xie Z *et al.* Kir6.1- and SUR2-dependent KATP
1249 overactivity disrupts intestinal motility in murine models of Cantu syndrome. *JCI*
1250 *Insight* 2020; **5**.
1251 51 Lee S, Kang BM, Shin MK *et al.* Chronic Stress Decreases Cerebrovascular
1252 Responses During Rat Hindlimb Electrical Stimulation. *Front Neurosci* 2015;
1253 **9**:462.
1254 52 Chiba S, Numakawa T, Ninomiya M, Richards MC, Wakabayashi C, Kunugi

1255 H. Chronic restraint stress causes anxiety- and depression-like behaviors,
1256 downregulates glucocorticoid receptor expression, and attenuates glutamate
1257 release induced by brain-derived neurotrophic factor in the prefrontal cortex.
1258 *Prog Neuropsychopharmacol Biol Psychiatry* 2012; **39**:112-119.
1259 53 Dion-Albert L, Dudek KA, Russo SJ, Campbell M, Menard C. Neurovascular
1260 adaptations modulating cognition, mood, and stress responses. *Trends*
1261 *Neurosci* 2023; **46**:276-292.
1262 54 Chen M, Ma S, Liu H *et al.* Brain region-specific action of ketamine as a
1263 rapid antidepressant. *Science* 2024; **385**:eado7010.
1264 55 Lee S, Kang BM, Kim JH *et al.* Real-time in vivo two-photon imaging study
1265 reveals decreased cerebro-vascular volume and increased blood-brain barrier
1266 permeability in chronically stressed mice. *Sci Rep* 2018; **8**:13064.
1267 56 Hsueh B, Chen R, Jo Y *et al.* Cardiogenic control of affective behavioural
1268 state. *Nature* 2023; **615**:292-299.
1269 57 Roy AK, Shehzad Z, Margulies DS *et al.* Functional connectivity of the
1270 human amygdala using resting state fMRI. *Neuroimage* 2009; **45**:614-626.
1271 58 Kim KJ, Ramiro Diaz J, Iddings JA, Filosa JA. Vasculo-Neuronal Coupling:
1272 Retrograde Vascular Communication to Brain Neurons. *J Neurosci* 2016;
1273 **36**:12624-12639.
1274 59 Jammal Salameh L, Bitzenhofer SH, Hanganu-Opatz IL, Dutschmann M,
1275 Egger V. Blood pressure pulsations modulate central neuronal activity via
1276 mechanosensitive ion channels. *Science* 2024; **383**:eadk8511.

1277 60 Moore CI, Cao R. The hemo-neural hypothesis: on the role of blood flow in
1278 information processing. *J Neurophysiol* 2008; **99**:2035-2047.
1279 61 Hou XH, Hyun M, Taranda J *et al.* Central Control Circuit for Context-
1280 Dependent Micturition. *Cell* 2016; **167**:73-86.e12.
1281 62 Tateno F, Sakakibara R, Kishi M *et al.* Brainstem Stroke and Increased Anal
1282 Tone. *Low Urin Tract Symptoms* 2012; **4**:161-163.
1283 63 Hassabis D, Kumaran D, Summerfield C, Botvinick M. Neuroscience-
1284 Inspired Artificial Intelligence. *Neuron* 2017; **95**:245-258.
1285 64 Park S, Whang M. Empathy in Human-Robot Interaction: Designing for
1286 Social Robots. *Int J Environ Res Public Health* 2022; **19**.
1287 65 Apfelbach R, Blanchard CD, Blanchard RJ, Hayes RA, McGregor IS. The
1288 effects of predator odors in mammalian prey species: a review of field and
1289 laboratory studies. *Neurosci Biobehav Rev* 2005; **29**:1123-1144.
1290 66 Bateman AW, Vos M, Anholt BR. When to defend: antipredator defenses and
1291 the predation sequence. *Am Nat* 2014; **183**:847-855.
1292 67 Liu Y, Wu Y, Yang Q. The impact of stress on the risk decision-making
1293 process. *Psychophysiology* 2024; **61**:e14595.
1294 68 Seo JS, Park JY, Choi J *et al.* NADPH oxidase mediates depressive behavior
1295 induced by chronic stress in mice. *J Neurosci* 2012; **32**:9690-9699.
1296 69 Khalil V, Faress I, Mermet-Joret N, Kerwin P, Yonehara K, Nabavi S.
1297 Subcortico-amygdala pathway processes innate and learned threats. *Elife* 2023;
1298 **12**.

1299 70 Yu XD, Zhu Y, Sun QX *et al.* Distinct serotonergic pathways to the amygdala
1300 underlie separate behavioral features of anxiety. *Nat Neurosci* 2022; **25**:1651-
1301 1663.
1302 71 Li X, Zhou L, Zhang X *et al.* Proteins secreted by brain arteriolar smooth
1303 muscle cells are instructive for neural development. *Mol Brain* 2022; **15**:97.
1304 72 Jin Y, Shi P, Wang Y *et al.* Precise control of embolic stroke with magnetized
1305 red blood cells in mice. *Commun Biol* 2022; **5**:136.
1306 73 Chao TH, Zhang WT, Hsu LM, Cerri DH, Wang TW, Shih YI. Computing
1307 hemodynamic response functions from concurrent spectral fiber-photometry
1308 and fMRI data. *Neurophotonics* 2022; **9**:032205.
1309 74 Oyarzabal EA, Hsu LM, Das M *et al.* Chemogenetic stimulation of tonic locus
1310 coeruleus activity strengthens the default mode network. *Sci Adv* 2022;
1311 **8**:eabm9898.
1312 75 Hou W, Yao J, Liu J *et al.* USP14 inhibition promotes recovery by protecting
1313 BBB integrity and attenuating neuroinflammation in MCAO mice. *CNS Neurosci*
1314 *Ther* 2023; **29**:3612-3623.
1315 76 Arakawa H, Arakawa K, Blanchard DC, Blanchard RJ. Scent marking
1316 behavior in male C57BL/6J mice: sexual and developmental determination.
1317 *Behav Brain Res* 2007; **182**:73-79.
1318 77 Arakawa H, Arakawa K, Blanchard DC, Blanchard RJ. A new test paradigm
1319 for social recognition evidenced by urinary scent marking behavior in C57BL/6J
1320 mice. *Behav Brain Res* 2008; **190**:97-104.

78 Borelli KG, Blanchard DC, Javier LK, Defensor EB, Brandao ML, Blanchard RJ. Neural correlates of scent marking behavior in C57BL/6J mice: detection and recognition of a social stimulus. *Neuroscience* 2009; **162**:914-923.

79 McQuaid RJ, Audet MC, Anisman H. Environmental enrichment in male CD-1 mice promotes aggressive behaviors and elevated corticosterone and brain norepinephrine activity in response to a mild stressor. *Stress* 2012; **15**:354-360.

80 Liu J, Li D, Huang J *et al.* Glutamatergic Neurons in the Amygdala Are Involved in Paclitaxel-Induced Pain and Anxiety. *Front Psychiatry* 2022; **13**:869544.

81 Warden MR, Selimbeyoglu A, Mirzabekov JJ *et al.* A prefrontal cortex-brainstem neuronal projection that controls response to behavioural challenge. *Nature* 2012; **492**:428-432.

ACKNOWLEDGMENTS

We thank Prof. Bo Li for editing the manuscript and providing suggestions. We thank Prof. Yanmei Tao and Dr. Xu Hu for sharing *Nestin-cre* and *Emx1-cre* mice. We thank Yi Zhu for sharing psychological knowledge to facilitate our understanding of data. We thank Yuxiao Niu for the KEGG map drawing. We thank Westlake University Laboratory Animal Resource Centre for guiding behaviour assays. We thank the Microscopy Core Facility of Westlake University for imaging guidance. We thank the Mass Spectrometry & Metabolomics Core Facility (MSMCF) of Westlake University for mass data

collection. We thank the Flow Cytometry Core Facility (FCCF) for cell sorting assistance. This work was supported by Westlake Laboratory of Life Sciences and Biomedicine (Project No. 202309002), Westlake University startup funding, the Westlake Education Foundation, Zhejiang, Key R&D Program of Zhejiang (2024SSYS0031), and the National Natural Science Foundation of China (project No. 32170961).

AUTHOR CONTRIBUTIONS

J.-M.J. conceived the project, designed the experiments, and supervised this study. J.Y.R. designed the key experiments, did primary experiments, obtained and organized the majority of original data, and wrote the manuscript draft. X.H.Q. participated in behavioural assay design and operations, siRNA cisterna magna injection, gut health inspection assay, BBB integrity inspection, caldesmon expression inspection, and cluster analysis of similarity index. Y.Y.Z. wrote the main MATLAB code for prediction framework. H.Q.X. participated in the Looming assay and VR_{eagle} assay, as well as in blood pressure measurement. D.D.Z. provided primer pairs of *Grin1*, raw data of electron microscope, and *SMA-creER:Grin1*$^{f/f}$ 40 cm OFT data. W.T.W. contributed to the writing of MATLAB code with Y.Y.Z.. B.R.Z. participated in the genotyping of mice and cell sorting. D.P.L. helped the mouse brain section.

CONFLICT OF INTERESTS

The authors declare no competing interests.

FIGURE LEGENDS

Fig.1 The negative emotion index. a Schematic diagrams of the home cage, OFT, and ARS. **b-c** BLA neuronal activation levels (**b**) and defecation bouts (**c**) under paradigms shown in **a**. Each dot represents one mouse. Student's t-test (**b**) and Mann-Whitney test (**c**) were used. **** indicates P<0.0001. **d** Linear correlation analysis between **b** and **c**. The original data were from **b** and part of **c**. **e** Time spent by mice in the center area of the OFT's box. Each dot represents one mouse. Student's t-test. **f** Total running distance by mice in the OFT. Each dot represents one mouse. Student's t-test. **g** Heatmap of mice's zone preference and defecation locations in the 40 cm OFT. **h** Statistical graph of **g**, data obtained from sixteen mice. **i** Schematic diagram of BLA chemogenetic inhibition during ARS. **j** Statistical graph of **i**. Each dot represents one mouse. Student's t-test. **k** Mice defecation bouts during BLA chemogenetic inhibition. Each dot represents one mouse. Mann-Whitney test. **l** Defecation rate and latency in the OFT. Number of mice is indicated in the figure. Gehan-Breslow-Wilcoxon test. **m** Time spent by mice in the center area of the OFT's box. Each dot represents one mouse. Student's t-test. **n** Total running distance by mice in the OFT. Each dot represents one mouse. Student's t-test. **o** Defecation bouts in the OFT following injection of the control virus. Each dot represents one mouse. Mann-Whitney test. Data are presented as mean ± SEM. See also Supplementary information Fig. S1.

1390 **Fig.2 GluN2D in SMCs regulates NVC and modulates negative emotions.**
1391 **a** Schematic diagram of the NsMJ within the NVU. **b** Schematic (top) and
1392 statistical graph (bottom) of RT-PCR. Each dot represents one mouse. **c**
1393 Schematic of RNA_{scope}. The inserted histogram shows the fluorescence
1394 intensity of the region indicated by the white arrows. The yellow dashed line
1395 indicates the boundary of the arteriole SMCs. **d** Schematic (left) and statistical
1396 graph (right) of MCA IF staining. Each dot represents one MCA. Six mice per
1397 group. Student's t-test. **** indicates P<0.0001. **e** Schematic diagram of the
1398 mouse whisker stimulation experiment. **f** Functional hyperemia in the S1BF
1399 during the whisker stimulation. **g** Statistical graph of the functional hyperemia
1400 plateau phase in **f**. Each dot represents one mouse. Student's t-test. ****
1401 indicates P<0.0001. **h** Schematic of the OFT combined with real-time neuronal
1402 activity, and rCBV monitoring in the BLA along with the negative emotion index
1403 monitor of freely moving mice. **i-j** rCBV (**i**) and Ca^{2+} (**j**) change in the BLA during
1404 the OFT. 0–900 seconds represents the duration of the OFT. **k** Statistical graphs
1405 of **i** and **j**. Each dot represents one mouse. Student's t-test. **l** Defecation bouts
1406 in every five minutes in a 40 cm OFT. Each dot represents one mouse. Mann-
1407 Whitney test. **m** Defecation rate and latency in the OFT. The number of mice is
1408 indicated in the figure. Gehan-Breslow-Wilcoxon test. **n** 1st 5 min rearing bouts
1409 in a 40 cm OFT. Each dot represents one mouse. Mann-Whitney test. **o**
1410 Defecation bouts in mice during OFTs of varying sizes and ARS. Each dot
1411 represents one mouse. Mann-Whitney test. **** indicates P<0.0001. Data are

1412 presented as mean±SEM. Data from **o** reuse the data of *Grin2d*$^{f/f}$ mice from **Fig.**
1413 **1c** for comparison. **l** and **o** use same raw data of defecation bouts of *Grin2d*$^{f/f}$
1414 and *SMA-creER:Grin2d*$^{f/f}$ mice. Data are presented as mean±SEM. See also
1415 Supplementary information Figs. S2-10.

1416

1417 **Fig.3 Multiple NVC dysfunction models lead to excessive negative**
1418 **emotions. a** Schematic diagram of the double cKO mice mating strategy. **b**
1419 Functional hyperemia in the S1BF during the whisker stimulation. **c** Statistical
1420 graph of the functional hyperemia plateau phase in **b**. Each dot represents one
1421 mouse. Student's t-test. **** indicates P<0.0001. **d** Defecation bouts in the OFT
1422 and ARS in mice. Each dot represents one mouse (the number in parentheses
1423 also indicates the number of mice). Mann-Whitney test. **e** Defecation rate and
1424 latency in the OFT. The number of mice is indicated in the figure. Gehan-
1425 Breslow-Wilcoxon test. **f** Schematic diagram of IF staining in the S1BF (left).
1426 The orange dashed line indicates the location of the magnified area in the upper
1427 right corner of the image. The right panel is a magnified view of the left
1428 schematic. NeuN^{-} cells refer to non-neuronal cells expressing COX-2 within the
1429 white dashed line in the left magnified image. Each dot represents one mouse.
1430 Student's t-test. **g** Functional hyperemia in the S1BF during the whisker
1431 stimulation. **h** Statistical graph of the functional hyperemia plateau phase in **g**.
1432 Each dot represents one mouse. Student's t-test. **i** Schematic (top) and
1433 statistical graph (bottom) of α-SMA. Each dot represents one mouse. Student's

1434 t-test. **j** Schematic diagram of the HFD-induced model. **k** Body weight changes
1435 of mice during HFD modelling. Each group sixteen mice. Student's t-test. ****
1436 indicates P<0.0001. **l** mice fat and lean changes during HFD modelling. Each
1437 dot represents one mouse. Student's t-test. **** indicates P<0.0001. **m**
1438 Functional hyperemia in the S1BF during the whisker stimulation. **n** Statistical
1439 graph of the functional hyperemia plateau phase in **m**. Each dot represents one
1440 mouse. Student's t-test. Data from **b-e** reuse the data of *Grin2d*$^{f/f}$ and *SMA-*
1441 *creER:Grin2d*$^{f/f}$ mice from **Fig. 2f, g, l, m** for comparison. NFD: normal fat diet.
1442 Data are presented as mean±SEM. See also Supplementary information Figs.
1443 S7, 11 ,12.

1444

1445 **Fig.4 Optogenetic stimulation of BLA SMCs. a** Schematic diagram of
1446 optogenetic stimulation in a freely moving mouse within the home cage. **b**
1447 Schematic diagram showing the implanted position of the fiber ceramic ferrule.
1448 **c** Schematic diagram illustrating the rCBV inhibition in the BLA under different
1449 optogenetic protocols. **d** Statistical graph of **c**. Each point represents the
1450 average change data from one mouse during the stimulation period. Student's
1451 t-test. **e** Schematic diagram of optogenetic stimulation in a freely moving mouse
1452 undergoing the OFT. **f** Schematic diagram illustrating the rCBV inhibition in the
1453 BLA during the OFT. **g** Statistical graph of **f**. Each point represents the average
1454 change data from one mouse during the stimulation period. Student's t-test. **h**
1455 Defecation bouts in freely moving mice during optogenetic stimulation in the

1456 OFT. Each point represents one mouse. Mann-Whitney test. **i** Defecation rate
1457 and latency in the OFT. The dashed line represents the median defecation
1458 latency. Twelve Control mice, and ten ChR2-overexpressing mice. Gehan-
1459 Breslow-Wilcoxon test. **j** Experimental design (top) of optogenetic stimulation
1460 (15 minutes) in a freely moving mouse within the home cage, and
1461 corresponding changes in BLA rCBF (bottom). **k** Statistical graph of **j**. Each
1462 point represents the average change from one mouse during optogenetic
1463 stimulation period. Student's t-test. **l** Defecation bouts of mice. Each point
1464 represents one mouse. Mann-Whitney test. **m** Schematic diagram of IF staining
1465 in the BLA following optogenetic stimulation in the home cage and OFT. Each
1466 point represents one mouse. Student's t-test. **n** Statistical graph of **m**. Each
1467 point represents one mouse. Student's t-test. Data are expressed as mean ±
1468 SEM. See also Supplementary information Figs. S13, 14.

1469

1470 **Fig.5 Caldesmon in SMCs regulates NVC and negative emotions. a** KEGG
1471 analysis of proteomic data from GluN2D IP products in SMCs. **b** IP products
1472 detection using GluN2D and caldesmon antibodies. **c** Schematic illustrating
1473 whole brain and BLA-specific caldesmon expression manipulation. **d**
1474 Schematic of caldesmon IF staining. **e** Statistical graph of **d**. Each dot
1475 represents one mouse. Student's t-test. **** indicates P<0.0001. **f**
1476 Representative image (upper) and quantitative analysis (lower) of *Cald*
1477 expression in the S1BF following whole-brain *Cald siRNA* injection. Each dot

1478 represents one mouse. Student's t-test. **g-h** Schematic of IF staining for
1479 caldesmon in the BLA (**g**) and ventromedial hypothalamus (VMH) (**h**) following
1480 BLA local *Cald* siRNA injection. **i** Statistical graph of **f-h**. Each dot represents
1481 one mouse. Student's t-test. **j** Functional hyperemia in the S1BF during the
1482 whisker stimulation. **k** Statistical graph of the functional hyperemia plateau
1483 phase in **j**. Each dot represents one mouse. Student's t-test. **l** Schematic of IF
1484 staining after OFT in mice injected with *Cald* siRNA into the BLA. **m** Statistical
1485 graph of **l**. Each dot represents one mouse. Student's t-test. **n** Defecation bouts
1486 in the OFT and ARS. Each dot represents one mouse. Mann–Whitney test. ****
1487 indicates P<0.0001. **o** Defecation rate and latency in the OFT. Number of mice
1488 is indicated in the figure. Gehan–Breslow–Wilcoxon test. Data from **n** and **o**
1489 reuse *Grin2d*$^{f/f}$ and *SMA-creER:Grin2d*$^{f/f}$ mice from **Fig. 2m, o** as controls. Data
1490 are presented as mean ± SEM. See also Supplementary information Figs. S15.

1491

1492 **Fig 6. Pharmacological enhanced NVC rescues consequences of NVC**
1493 **impairment. a** Schematic diagram of drug intraperitoneal injection and BLA
1494 local injection. **b-e** Effects of Het0016 administered via intraperitoneal injection
1495 (**b, c**) and BLA local injection (**d, e**) on the negative emotion index in the OFT.
1496 Each dot represents one mouse. **b, d** use Mann-Whitney test. **c, e** use Gehan-
1497 Breslow-Wilcoxon test. **** indicates P<0.0001. **f** Effects of Het0016 on 1st 5
1498 min rearing bouts. Each dot represents one mouse. Mann-Whitney test. **g**
1499 Defecation bouts of *Pdgfrβ-creER:Acta2*$^{f/f}$ mice after BLA local Het0016

1500 injection in the OFT. Mann-Whitney test. **k** Defecation rate and defecation
1501 latency of *Pdgfrβ-creER:Acta2*$^{f/f}$ mice in the OFT after BLA local Het0016
1502 injection. The number of mice is indicated in the figure. Gehan-Breslow-
1503 Wilcoxon test. **i** Effects of Het0016 on 1st 5 min rearing bouts. Each dot
1504 represents one mouse. Mann-Whitney test. Data are presented as mean ± SEM.
1505 See also supplementary information, Figs. S16, 17.

1506

1507 **Fig 7. Topology-Based estimation framework. a-b** SSIM-based unbiased
1508 classification of stress levels for seven standard contexts in control (**a**) and NVC
1509 deficiency mice (**b**). **c-h** The predicted position of every single treatment in the
1510 unbiased classification system. Black font represents *Grin2d*$^{f/f}$ mice. Pink font
1511 represents *SMAcreER:Grin2d*$^{f/f}$ mice. Red font represents *Cald*-KD mice (**e**)
1512 and ChR2^{+} mice (**f**). Pink arrow presents the location of *SMAcreER:Grin2d*$^{f/f}$
1513 mice, *Cald*-KD mice, and ChR2^{+} mice with unbiased classification in the
1514 Topology-Based estimation framework. See also Supplementary information
1515 Figs. S18, S19.

1516

1517 **Fig. 8 NVC deficiency prompted an early relaxation of defense upon**
1518 **predator-like threat. a-d** Looming assay. Temporal profile of locomotion speed
1519 dynamics of the two genotypic mice before (blue) and during (yellow)
1520 stimulation in **a**. Heatmap that profiled the locomotion speed dynamics for 30

1521 seconds in **b**. The yellow box marks the 3-sec looming duration. Cumulative
1522 time used for relaxation from a freezing status following looming stimulation in
1523 **c**. Rearing bouts of each group in **d**. Fifteen mice for each group. **e-g** VR_{eagle}
1524 stimulation. Temporal changes of the normalized pupil size and locomotion
1525 speed during and after VR_{eagle} stimulation in **e**. Eagle call only present during
1526 the first 1.5s (blue) and eagle started to dive at 1.5 second (yellow).
1527 Representative images of VR_{eagle} video and mouse eye with pupil clear
1528 visualized. The statistical data of the defensive offset phase for **e** in **f**. The
1529 statistical data of pupil size full-recovery latency and looming locomotion full-
1530 recovery latency in **g**. For VR_{eagle}, seven mice for each group; for Looming,
1531 fifteen mice for each group. **h-l** Cat_{video} assay. The locomotion pattern during
1532 the Cat_{video} assay in **h**. Black bar marks retreat behavior; magenta lines indicate
1533 tail rattling. Two vertical dash lines highlight the time points when the cat
1534 appeared and pounced. Mouse numbering is on the left. Quantification of
1535 retreat behaviors of *Grin2d*$^{f/f}$ mice before and after cat appearance in **i**. Retreat
1536 rate of two groups upon in Cat_{video} stimulation in **j**. Retreat rate referred to the
1537 fraction of mice that exhibited at least one retreat behavior of total mice.
1538 Cumulative retreat time curve in **k**. Quantification of tail rattling times in **l**. Twelve
1539 mice for each group. Student's t-test. Data are presented as mean ± SEM. See
1540 also supplementary information, Fig. S20.

1541

1542 **Fig 9. NVC-deficient mice show hypo-responses to aggressive social**
1543 **stress. a** Diagram of a home cage from a side view. **b** Total fighting time. each
1544 dot indicates one mouse. **c-d** Predicted positions of the two genotypic mice
1545 experience aggressive social stress. **e** Total time of staying with CD1 mouse in
1546 the small space. **f-g** Flee rate of *Grin2d*$^{f/f}$ and *SMA-creER:Grin2d*$^{f/f}$ mice
1547 (counted as per mouse) after fighting in **f**, and the normalized flee rate (counted
1548 as per fight event) after each fighting in **g**. Numbers in the graph indicates
1549 mouse number (**f**) and events (**g**). **h** Sniffing duration. Eight mice for *Grin2d*$^{f/f}$
1550 and ten mice for *SMA-creER:Grin2d*$^{f/f}$. Student's t-test. In **c-d**, black font
1551 represents *Grin2d*$^{f/f}$ mice in **Fig. 7**. Blue (**c**) and pink (**d**) font represent *Grin2d*$^{f/f}$
1552 mice (**c**) and *SMAcreER:Grin2d*$^{f/f}$ mice (**d**). Blue (**c**) and pink (**d**) arrow present
1553 the location of *Grin2d*$^{f/f}$ mice (**c**) and *SMAcreER:Grin2d*$^{f/f}$ mice (**d**) with unbiased
1554 classification in the Topology-Based estimation framework. Data are presented
1555 as mean ± SEM.

1556

1557 **Fig. 10 Enhanced NVC in transgenic mouse model prevents strong CRS-**
1558 **induced NVC dysfunction and resistance emotional distress. a** Schematic
1559 of RNA_{scope} of *Glrb* mRNA expression in venous SMCs. **b** Statistical graph of **a**.
1560 Each dot represents a vessel. Four mice per group. Mann-Whitney test. ****
1561 indicates P<0.0001. **c** GlyRβ expression in venous SMCs. **d** Statistical graph
1562 of **c** (comparison between arterioles and venules in control mice). Each dot
1563 represents a vessel. Four mice per group. Mann-Whitney test. **e** Statistical

1564 graph of **c** (comparison between venules of control and cKO mice). Each dot
1565 represents a vessel. Four mice per group. Student's t-test. **f** Schematic (top)
1566 and quantification (bottom) of *Glrb* expression in Pdgfrβ$^+$ cells from the cortex.
1567 Each dot represents one mouse. Student's t-test. **g** Co-localization of GlyRβ
1568 with Gephyrin in HU-vSMC. The upper right panel shows the co-localization
1569 rate. **h** Co-localization of GlyRβ protein with glycinergic axon terminals. The
1570 orange dashed box indicates the zoom-in area in the upper right. Lower right is
1571 histogram displays the fluorescence intensity across the region indicated by the
1572 white arrow above. **i** Sequential electron microscopy sections of a ascending
1573 venule in mouse cerebral cortex. White arrows indicate structural contacts
1574 between axonal terminal and venous SMCs. **j** Functional hyperemia in the
1575 S1BF during the whisker stimulation. **k** Statistical graph of the functional
1576 hyperemia plateau phase in **j**. Each dot represents one mouse. Student's t-test.
1577 **l** NVC-neutrality mice mating strategy. **m** Defecation bouts during the OFT and
1578 ARS. Each dot represents one mouse. Mann-Whitney test. **** indicates
1579 P<0.0001. **n** Defecation rate and defecation latency of mice in the OFT. The
1580 number of mice is indicated in the figure. Gehan-Breslow-Wilcoxon test. **o**
1581 Schematic diagram of the CRS model. **p** Fecal appearance of mice following
1582 CRS. BS: Bristol score. **q** Bristol score and defecation bouts during CRS
1583 modelling. Fiftheen mice per group. Mann-Whitney test. **** indicates P<0.0001.
1584 **r** Immobility time of mice in the FST. Each dot represents one mouse. Student's
1585 t-test. **** indicates P<0.0001. Data from **j, k, m, n** reuse the data of *Pdgfrβ-*

1586 *creER:Grin2d*$^{f/f}$ mice from **Fig. 3b-e** for comparison. Data are presented as

1587 mean ± SEM. See also supplementary information, Figs. S21-27.

1588

1589 **SUPPLEMENTARY INFOEMATION**

1590 **Supplementary figure legends**

1591 **Fig. S1 Schematic illustration of BLA IF staining in conditions shown in**

1592 **Fig. 1a, b.**

1593

1594 **Fig. S2 Supplementary data for *Grin2d-cKO*. a** Schematic of RNA_{scope} of

1595 *Grin1* and *Grin2d* expression in the cerebellum. **b** Statistical graph of **a**. Each

1596 dot represents one mouse. **c-d** Schematic (top) and statistical graph (bottom)

1597 of GluN2D experiments in cerebral SMCs of mouse brain parenchyma (**c**) and

1598 whole cortex lysis (**d**). Each point represents one mouse. Student's t-test. **e**

1599 Schematic illustration (top) and quantitative analysis (bottom) of GluN2D. Each

1600 dot represents one mouse. Student's t-test. **** indicates P<0.0001. Data are

1601 presented as mean ± SEM.

1602

1603 **Fig. S3 Vascular topology in the BLA of the mouse. a** The schematic ventral

1604 view illustration of vascular topology is adapted from Figure 14.1 on page 460

1605 of book *The Mouse Nervous System.* Translucent gray area indicates BLA. **b**

1606 The coronal view of the BLA. Green, yellow, and red lines indicate arterial

1607 distribution in the BAa, and BAv, and LA part of the BLA, respectively.

1608

1609 **Fig. S4 Validation for detecting plasma rhodamine fluorescence intensity.**
1610 **a** Real-time fluorescence intensity measurement following retro-orbital
1611 intravenous injection of various concentrations of rhodamine. **b** Linear
1612 correlation statistical graph of **a**. Each point represents the average
1613 fluorescence intensity from 120 to 150 seconds post-injection for a specific
1614 rhodamine concentration. **c** Real-time fluorescence intensity measurements
1615 following retro-orbital intravenous injection of 5 mg/mL rhodamine. The
1616 experimental period ranged from 900 to 3600 seconds post-injection.

1617

1618 **Fig. S5 Neuronal activation in the BLA of *Grin2d-cKO* mice. a** Schematic
1619 illustration of IF staining in the BLA after the OFT. **b** Statistical graph of **a**. Each
1620 dot represents one mouse. Control mice data in **b** reuse data from **Fig. 1b** for
1621 comparison. Student's t-test. Data are presented as mean ± SEM.

1622

1623 **Fig. S6 Supplementary data on baseline rCBF and OFT in *Grin2d-cKO***
1624 **mice. a** rCBF in the BLA of mice before entering the OFT box. Each dot
1625 represents one mouse. Student's t-test. **b** Total running distance by mice during
1626 the OFT. Each dot represents data from one mouse. Student's t-test. **c** Time
1627 spent by mice in the central area of the OFT box. Each dot represents data from
1628 one mouse. Student's t-test. Data are presented as mean ± SEM.

1629

1630 **Fig. S7 Verification of mouse metabolic status, gut health, and BBB**
1631 **integrity. a-g** Food consumption, water intake, number of fecal pellets, daily
1632 fecal weight, weight per pellet, urine output, body weight changes, and blood
1633 pressure measured in the home cage. Each data point in figures **a-f** represents
1634 the average value for four mice within a cage. Each data point in figures **g-h**
1635 represents an individual mouse. Mann-Whitney test was applied for
1636 nonparametric data analysis, while Student's t-test was used otherwise. **i**
1637 Schematic illustration of mouse intestinal length, appearance, and HE staining
1638 under microscopy. **j-n** Statistical graphs of **i**. Shown are the body weight (**j**),
1639 intestinal length (**k**), intestinal length to body weight ratio (**l**), and total defecation
1640 count over 24 hours for 8-week-old experimental mice (**m**). Each data point
1641 represents one mouse. Student's t-test. **o** Appearance examination of the brain
1642 following retro-orbital intravenous injection of Evans Blue. **p** Statistical graph of
1643 **o**. Each data point represents one mouse. Student's t-test. Data are presented
1644 as mean ± SEM.

1645

1646 **Fig. S8 SMC's marker protein validation in *Grin2d-cKO* mice. a** Schematic
1647 illustration (top) and quantitative analysis (bottom) of α-SMA. Each dot
1648 represents one mouse. Student's t-test. **b** Statistical graph of Smoothelin IF
1649 staining from **Fig. 2d**. Each dot represents one MCA. Four mice per group.
1650 Student's t-test. Data are presented as mean ± SEM.

1651

1652 **Fig. S9 Validation of GluN2D expression levels in peripheral organs. a**
1653 Low-magnification schematic diagrams of tissue sections from the heart, liver,
1654 spleen, lung, kidney, small intestine, and bladder of *SMA-creER:Ai14* mice (top).
1655 The yellow dashed box indicates the area enlarged (bottom). White arrows
1656 indicate the regions of interest for fluorescence intensity analysis in **b**. **b**
1657 Fluorescence intensity distribution in the regions indicated by the white arrows
1658 in **a**. **c** Statistical analysis of GluN2D IF staining intensity in GluN2D-positive
1659 cells and SMCs from tissue sections of **a**. Each dot represents one mouse.
1660 Student's t-test. **** indicates P<0.0001. Data are presented as mean ± SEM.

1661

1662 **Fig. S10 The effect of tamoxifen on NVC. a** Functional hyperemia in the S1BF
1663 during the whisker stimulation. **b** Statistical graph of the functional hyperemia
1664 plateau phase in **a**. Each data point represents one mouse. Student's t-test.
1665 Data are presented as mean ± SEM.

1666

1667 **Fig. S11 IF staining of penetrating arteries in the mouse cerebral cortex.**
1668 CD31 is the marker of endothelial cells.

1669

1670 **Fig. S12 Supplementary figure for HFD modelling. a** Statistical graph of daily

food consumption per cage. Each point represents the average of five mice per cage. Student's t-test. **b** Appearance examination of the brain following retro-orbital intravenous injection of Evans Blue (left) and statistical graph (right) of left. Each point represents one mouse. Student's t-test. Data are presented as mean ± SEM.

Fig. S13 BLA blood spectral energy analysis. a Representative image of mouse BLA blood spectral energy. **b** Statistical graph of **a**. Each data point represents one mouse. Student's t-test. Data are presented as mean ± SEM.

Fig. S14 Optogenetic stimulation supplementary data. a Total running distance by mice in the OFT. Each dot represents data from one mouse. Student's t-test. **b** Time spent by mice in the center area of the OFT's box. **c** Schematic diagram of IF staining for the BLA after optogenetic stimulation in the home cage. Stroke area Hif-1α from stroke model mice served as a positive control. **d** Statistical graph of **c**. Each data point represents one mouse. Student's t-test. Data are presented as mean ± SEM.

Fig. S15 S1BF *Cald* KD does not impact emotional responses. a Schematic illustration showing the injection site of *Cald* siRNA in the S1BF and its spatial relationship with the BLA (orange dashed line). **b-c** Schematic diagram of IF

staining in the S1BF (**b**) BLA (**c**) after *Cald* siRNA injection into the S1BF. **d** Statistical analysis of **b-c**. Each dot represents one mouse. Student's t-test. **e** The defecation bouts in the OFT. Each dot represents one mouse. Mann-Whitney test. **f** Defecation rate and latency in the OFT. The number of mice is indicated in the figure. Gehan-Breslow-Wilcoxon test. Data are presented as mean ± SEM.

Fig. S16 Het0016 concentration test. a Effects of different concentrations of Het0016 on the defecation bouts in ARS. Each dot represents one mouse. Mann-Whitney test. **b** Functional hyperemia in the S1BF during the whisker stimulation. **c** Statistical graph of the functional hyperemia plateau phase in **b**. Each dot represents one mouse. Paired Student's t-test. Data are presented as mean±SEM.

Fig. S17 The effects of Het0016 in HFD-induced obese mice. a The defecation bouts in the OFT in HFD-induced obese mice. Each dot represents one mouse. Mann-Whitney test. **b** Defecation rate and latency in the OFT in HFD-induced obese mice. The number of mice is indicated in the figure. Gehan-Breslow-Wilcoxon test. Data are presented as mean±SEM.

Fig. S18 Schematic diagrams of behavioural apparatus and setups. a

Diagram of the complex OFT chamber. **b** Diagram of the Looming assay setup. **c** Diagram of the VR_{eagle} assay. **d** Diagram of the Cat_{video} assay.

Fig. S19 Neuronal activity changes and defecation bouts of mice in different contexts. a Schematic diagram of neuronal activity changes and c-Fos activation topography in the BLA of mice across different behavioral paradigms. Each dot represents one mouse. Student's t-test. Data are presented as mean ± SEM. **b** Normalized defecation bouts per 15 minutes in different contexts. Each dot represents one mouse. Mann-Whitney test. Social: aggressive social stress assay. **c** P_value of **b**. Schematic topological diagram from **a** reuse the diagram from **Fig.7a, b**. Data are presented as mean ± SEM.

Fig. S20 Supplementary data from the Looming and VR_{eagle} assays. a Statistical analysis of mice's locomotion speed before stimulation in the Looming assay. Each dot represents one mouse. Student t-test. **b** Statistical analysis of mice's locomotion speed before stimulation in the VR_{eagle} assay. Each dot represents one mouse. Student t-test. **c** Statistical analysis of mice's pupil size before stimulation in the VR_{eagle}. Each dot represents one mouse. Student t-test. **d** Statistical analysis of mice's pupil size at the last moment of stimulation in the VR_{eagle}. Each dot represents one mouse. Student t-test. Data are presented as mean ± SEM.

1734

1735 **Fig. S21 The expression level of *Glrb* in the transcriptome database.** vSMC
1736 refers to venous SMCs, aaSMC refers to arteriolar SMCs, and aSMC refers to
1737 arterial SMCs. Data are presented as mean ± SEM.

1738

1739 **Fig. S22 Functional hyperemia and behavioral supplementary data in**
1740 **SMC-specific *Glrb-cKO* mice. a** Functional hyperemia in the S1BF during the
1741 whisker stimulation. **b** Statistical graph of the functional hyperemia plateau
1742 phase in **a**. Each data point represents one mouse. Student's t-test. **c**
1743 Defecation bouts during ARS. Each data point represents one mouse. Mann-
1744 Whitney test. Data are presented as mean ± SEM.

1745

1746 **Fig. S23 Pinacidil inhibits NVC enhancement. a** Schematic illustration of
1747 intraperitoneal and BLA local injection of pinacidil. **b** Functional hyperemia in
1748 the S1BF during the whisker stimulation. **c** Statistical graph of the functional
1749 hyperemia plateau phase in **b**. Each dot represents one mouse. Paired
1750 Student's t-test. **d** Absolute rCBF in the S1BF of mice before the whisker
1751 stimulation. Each dot represents one mouse. Paired Student's t-test. **e-f**
1752 Defecation bouts of mice during ARS after intraperitoneal injection (**e**) and BLA
1753 local injection (**f**) of pinacidil. Each dot represents one mouse. Mann–Whitney
1754 test. Data are presented as mean ± SEM.

1755

1756 **Fig. S24 Statistics of the time spent in the open arms of the EMP (left) and**
1757 **fecal pellet quality (right) in mice after CRS modelling.** Each dot represents
1758 one mouse. Student's t-test was used for the left panel statistics, and Mann-
1759 Whitney test was used for the right panel statistics. BS: Bristol score. Data are
1760 presented as mean ± SEM.

1761

1762 **Fig. S25 Defecation bouts of mice in ARS.** Each dot represents one mouse.
1763 Mann-Whitney test. **** indicates P<0.0001. *Glrb*$^{f/f}$ and *Pdgfrβ-creER:Glrb*$^{f/f}$
1764 data are reused from **Fig. 10m** as controls. Data are presented as mean ± SEM.

1765

1766 **Fig. S26 Locomotion, anxiety-like, and weight of NVC-enhancement mice.**
1767 **a** Total running distance by mice in the OFT. Each dot represents one mouse.
1768 Student's t-test. **b** Time spent by mice in the center area of the OFT's box. Each
1769 dot represents one mouse. Student's t-test. **c** Body weight changes of mice
1770 during the CRS modelling. Fifteen mice per group. Student's t-test. Data are
1771 presented as mean ± SEM.

1772

1773 **Fig. S27 BBB integrity following the CRS modelling. a** Schematic illustration
1774 of IF staining in the S1BF and the BLA. **b** Statistical graph of **a**. Each dot

represents one mouse. Student's t-test. Data are presented as mean ± SEM.

Fig. S28 Schematic illustration of the BLA-Bar axis. Dotted arrows and grey font represent inferred neuronal circuits or functions.

Supplementary tables

Supplementary Table S1. P-value of Defecation rate-latency curve

Sub table 1 for **Fig. 2m**

P_value	1	2	3	4	5	6
1	1	0.0031	0.0019	****	****	****
2		1	0.1934	0.3581	0.1384	0.1189
3			1	0.8685	0.3193	0.3458
4				1	0.1585	0.1083
5					1	0.9278
6						1

1. OFT_40 *Grin2d*$^{f/f}$
2. OFT_35 *Grin2d*$^{f/f}$
3. OFT_10 *Grin2d*$^{f/f}$
4. OFT_40 *SMA-creER:Grin2d*$^{f/f}$
5. OFT_40 *SMA-creER:Grin2d*$^{f/f}$

1788 6. OFT_40 *SMA-creER:Grin2d*$^{f/f}$

1789 **** indicates P<0.0001

1790

1791 Sub table 2 for **Fig. 3e**

P_value	1	2	3	4	5	6	7	8	9	10	11	12
1	1	****	0.0002	0.0823	0.0005	0.8480	****	0.4924	0.4906	****	0.5680	****
2		1	0.7333	0.0092	0.7209	0.0002	0.0786	0.0010	0.0043	0.4279	0.0010	0.2679
3			1	0.0047	0.7747	0.0001	0.2580	0.0014	0.0028	0.7549	0.0010	0.4218
4				1	0.0130	0.1038	****	0.2713	0.2961	0.0009	0.0548	0.0005
5					1	0.0004	0.2596	0.0042	0.0078	0.9480	0.0022	0.5377
6						1	****	0.5712	0.5970	****	0.4793	****
7							1	****	****	0.2935	0.0003	0.8118
8								1	0.9720	0.0001	0.2299	0.0001
9									1	0.0008	0.2695	0.0005
10										1	0.0003	0.5583
11											1	0.0005
12												1

1792 1. *Grin2d*$^{f/f}$

1793 2. *SMA-creER:Grin2d*$^{f/f}$

1794 3. *Pdgfrβ-creER:Grin2d*$^{f/f}$

1795 4. *Grin1*$^{f/f}$

1796 5. *SMA-creER:Grin1$^{f/f}$*

1797 6. *Ptgs2$^{f/f}$*

1798 7. *Emx1-cre:Ptgs2$^{f/f}$*

1799 8. *SMA-creER:Ptgs2$^{f/f}$*

1800 9. *Acta2$^{f/f}$*

1801 10. *Pdgfrβ-creER:Acta2$^{f/f}$*

1802 11. NFD

1803 12. HFD

1804 **** indicates P<0.0001

1805

1806 Sub table 3 for **Fig. 5p**

P_value	1	2	3	4	5	6	7
1	1	****	0.9518	****	****	0.0008	****
2		1	0.0001	0.6713	0.4083	0.7646	0.4077
3			1	****	****	0.0009	****
4				1	0.5745	0.8881	0.9999
5					1	0.99990	0.6926
6						1	0.6353
7							1

1807 1. *Grin2d$^{f/f}$*

1808 2. *SMA-creER:Grin2d$^{f/f}$*

1809 3. Scramble

1810 4. *Cald* KD (Brain)

1811 5. *Cald* KD (BLA)

1812 6. Scramble+ *SMA-creER:Grin2d*$^{f/f}$

1813 7. *Cald* KD (BLA) + *SMA-creER:Grin2d*$^{f/f}$

1814 **** indicates P<0.0001

1815

1816 Sub table 4 for **Fig. 6c**

P_value	1	2	3	4
1	1	0.1650	****	0.6470
2		1	****	0.2934
3			1	****
4				1

1817 1. *Grin2d*$^{f/f}$ +Saline

1818 2. *Grin2d*$^{f/f}$ +Het0016

1819 3. *SMA-creER:Grin2d*$^{f/f}$+Saline

1820 4. *SMA-creER:Grin2d*$^{f/f}$+ Het0016

1821 **** indicates P<0.0001

1822

1823 Sub table 5 for **Fig. 6e**

P_value	1	2	3	4
1	1	0.0679	0.0003	0.2123
2		1	****	0.3173
3			1	****
4				1

5. *Grin2d*$^{f/f}$ +Saline
6. *Grin2d*$^{f/f}$ +Het0016
7. *SMA-creER:Grin2d*$^{f/f}$+Saline
8. *SMA-creER:Grin2d*$^{f/f}$+ Het0016

**** indicates P<0.0001

Sub table 6 for **Fig. 10n**

P_value	1	2	3	4
1	1	0.0012	0.6285	0.4703
2		1	0.0035	0.0244
3			1	0.2637
4				1

1. Floxp
2. *Pdgfrβ-creER:Grin2d*$^{f/f}$
3. *Pdgfrβ-creER:Glrb*$^{f/f}$

4. *Pdgfrβ-creER:Grin2d$^{f/f}$:Glrb$^{f/f}$*

**** indicates P<0.0001

Supplementary Table S2. SSIM for Fig.7

SSIM	HC	OFT_40	complex OFT	ARS	Cat_{video}	Looming	VR_{eagle}
HC	1	0.0359	0	0	0.0019	0.0015	0.0205
OFT_40		1	0.0038	0.0011	0.2150	0.1550	0.79800
complex OFT			1	0.2190	0.1050	0.0461	0.0002
ARS				1	0.0183	0.0084	0
Cat_{video}					1	0.9440	0.0778
Looming						1	0.0542
VR_{eagle}							1

Supplementary Table S3. Mice information

Abbreviation	Full name	Source
Ai32	B6;129S-Gt(ROSA)26Sortm32(CAG-COP4*H134R/EYFP)Hze/J	Hailan Hu, Zhejiang University

Nestin-cre	B6.Cg-Tg(Nes-cre)1Kln/J	Yanmei Tao and Xu Hu, Hangzhou Normal University/ Southeast University
Emx1-cre	B6.129S2-Emx1tm1(cre)Krj/J	Yanmei Tao and Xu Hu, Hangzhou Normal University/ Southeast University
SMA-creER	Tg(Acta2-cre/ERT2)12Pcn	Bo Zhou, ShanghaiInstitutes for Biological Sciences, Chinese Academy of Sciences
Pdgfrβ-creER	Tg(Pdgfrb-cre/ERT2)6096Rha	Xiang Yu, Peking University
Ai47	Gt(ROSA)26Sortm47(CAG-EGFP*)Hze	Zilong Qiu, Chinese Academy of Sciences Center for Excellence in Brain Science and Intelligence Technology, Chinese Academy of Sciences.

Ai14	B6.Cg-Gt(ROSA)26Sortm14(CAG-tdTomato)Hze/J	Woo-Ping Ge, Chinese Institute of Brain Research (CIBR)
Grin2d	B6/JGpt-Grin2dem1Cflox/Gpt	GemPharmatech
Grin1	Grin1tm2Stl	Yangang Sun, Chinese Academy of Sciences Center for Excellence in Brain Science and Intelligence Technology, Chinese Academy of Sciences
Ptgs2	C57BL/6JCya-Ptgs2em1flox/Cya	Cyagen
Acta2	C57BL/6JGpt-Acta2em1Cflox/Gpt	GemPharmatech
Glrb	C57BL/6JGpt-Glrbem1Cflox/Gpt	GemPharmatech

Supplementary Table S4. Antibodies information

Name	Host	Cat#	Dilution	Company

Anti-NMDAR2D Antibody	Mouse	MAB5578	1:400 (IF) 1:2,500 (WB) 1:1,000 (IP)	Merck
Anti-Smoothelin antibody	Rabbit	ab219652	1:400 (IF)	abcam
α-Smooth Muscle Actin (ACTA2) Rabbit mAb	Rabbit	A17910	1:2,500 (WB)	ABclonal
ACE2 Recombinant Rabbit Monoclonal Antibody (SN0754)	Rabbit	MA5-32307	1:400 (IF)	Invitrogen
Gephyrin Polyclonal Antibody	Rabbit	PA5-29036	1:400 (IF)	Invitrogen
BD Pharmingen™ Purified Rat Anti-Mouse CD31	Rat	557355	1:200 (IF)	BD
Anti-NeuN purified Antibody	Guinea Pig	ABN90P	1:800 (IF)	Merck
COX2/PTGS2 Rabbit pAb	Rabbit	A1253	1:400 (IF)	ABclonal
c-Fos antibody	Rabbit	226 003	1:1,000 (IF)	SYSY
Recombinant Alexa Fluor® 488 Anti-Caldesmon/CDM antibody	Rabbit	ab208116	1:400 (IF)	abcam

			1:2,500 (WB)	
iFluor™ 488 Conjugated Goat anti-mouse IgG polyclonal Antibody	Goat	HA1125	1:400 (IF)	HUABIO
Mouse Aminopeptidase N/CD13 Antibody	Goat	AF2335	1:200 (IF)	R&D
CD140b (PDGFRB) Monoclonal Antibody (APB5), APC, eBioscience™	Rat	17-1402-82	1:50 (FCM)	Invitrogen
Mice IgG	Mouse	A7028	1:1,000 (IP)	Beyotime
Donkey anti-Mouse IgG (H+L) ReadyProbes™ Secondary Antibody, Alexa Fluor™ 488	Donkey	R37114	1:1,000 (IF)	Invitrogen
Donkey anti-Rabbit IgG (H+L) ReadyProbes™ Secondary Antibody, Alexa Fluor™ 488	Donkey	R37118	1:1,000 (IF)	Invitrogen
Donkey anti-Rabbit IgG (H+L) Highly Cross-Adsorbed Secondary Antibody, Alexa Fluor™ 546	Donkey	A10040	1:1,000 (IF)	Invitrogen

Donkey anti-Rat IgG (H+L) Highly Cross-Adsorbed Secondary Antibody, Alexa Fluor™ 488	Donkey	A21208	1:1,000 (IF)	Invitrogen
Donkey anti-Rat IgG (H+L) Highly Cross-Adsorbed Secondary Antibody, Alexa Fluor™ 555	Donkey	A78945	1:1,000 (IF)	Invitrogen
Donkey anti-Rat IgG (H+L) Highly Cross-Adsorbed Secondary Antibody, Alexa Fluor™ Plus 647	Donkey	A48272	1:1,000 (IF)	Invitrogen
Alexa Fluor® 647 AffiniPure™ Donkey Anti-Guinea Pig IgG (H+L)	Donkey	706-605-148	1:1,000 (IF)	Jackson ImmunoResearch
β-Tubulin Mouse mAb	Mouse	AC021	1:5,000 (WB)	ABclonal
Goat Anti-Mouse IgG, HRP Conjugated	Goat	CW0102	1:10,000 (WB)	CWBIO
Goat Anti-Rabbit IgG, HRP Conjugated	Goat	CW0103	1:10,000 (WB)	CWBIO
DDDDK-Tag Rabbit mAb	Rabbit	AE063	1:400 (IF)	ABclonal

Hif-1α	Rabbit	ER1802-41	1:100 (IF)	HUABIO

Supplementary Table S5. Primer pairs information

Name		Sequence
Grin1	F	AAGAACCTGCAGCAGTACCA
	R	GCAGCAGGACTCATCAGTGT
Grin2a	F	TCAGGGACTTTGGAAAACGCT
	R	AAGTCATGCAGGGTTGGTTG
Grin2b	F	ACTAACTATCAATGAAGAACGGT
	R	CCAGACCCCAGAGTAACCA
Grin2c	F	TGTGGGCCTTCTTCGCTGTCATCT
	R	TGCCATTAGGTACCGTGCCAAAAC
Grin2d	F	TGGAGGAGTACGACTGGACAT
	R	CGCACTGACACTACGGAGC
Grin3a	F	CTGCACACCAGTCAGAGGTT
	R	TTCGTTGGTTGTCGTGACTC

Grin3b	F	TGGGGGTCTACCACTTGTCA
	R	TGGATCTTCTGGCTCGTGTG
Glrb	F	TTCAAAGGCATTCCTGTTGATGT
	R	TGAGCCTCTGAAGTCACTAGG
Cald	F	GCCGTTCAAGTGCTTCACTC
	R	TGTCAATCTTGGAGACTACTGCT
18s	F	CGGACACGGACAGGATTGACA
	R	CCAGACAAATCGCTCCACCAACTA
Cald (siRNA)	F	GUUUGAUCCGACCAUAACAGA
	R	UGUUAUGGUCGGAUCAAACUC

Supplementary Video

Supplementary Video S1. Topological distribution of arterioles in the BLA.

Supplementary Video S2. VR_{eagle} stimulation assay.

Supplementary Video S3. Cat_{video} stimulation assay.

Figure 1

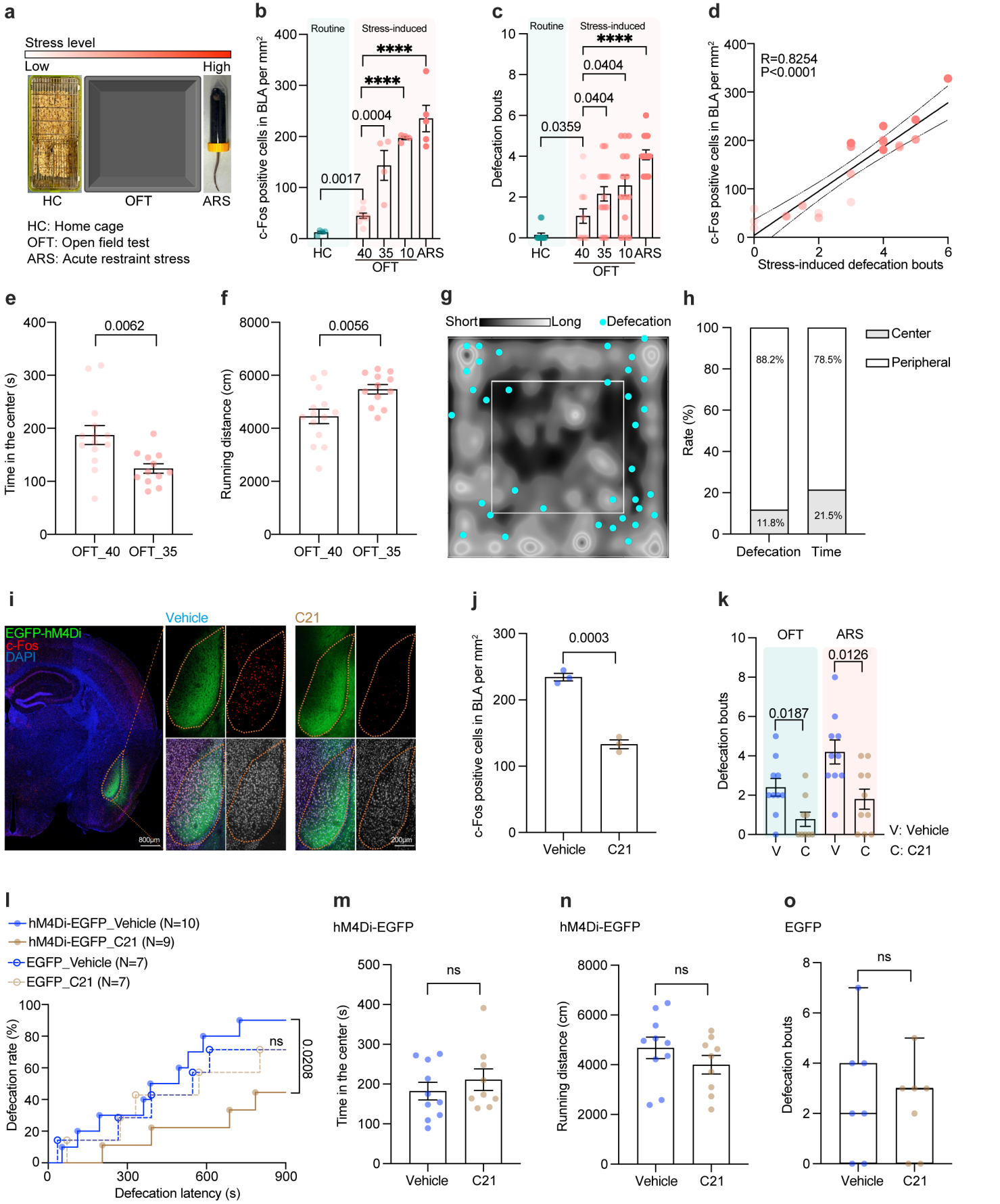
a
Stress level
Low
High
HC
OFT
ARS
HC: Home cage
OFT: Open field test
ARS: Acute restraint stress
b
Routine
Stress-induced
c-Fos positive cells in BLA per mm²
0.0017
0.0004
****
****
HC
40
35
10
ARS
OFT
c
Routine
Stress-induced
Defecation bouts
0.0359
0.0404
0.0404
****
d
R=0.8254
P<0.0001
c-Fos positive cells in BLA per mm²
Stress-induced defecation bouts
e
Time in the center (s)
0.0062
OFT_40
OFT_35
f
Running distance (cm)
0.0056
OFT_40
OFT_35
g
Short
Long
Defecation
h
Rate (%)
Center
Peripheral
88.2%
11.8%
78.5%
21.5%
Defecation
Time
i
Vehicle
C21
EGFP-hM4Di
c-Fos
DAPI
800μm
200μm
j
c-Fos positive cells in BLA per mm²
0.0003
Vehicle
C21
k
OFT
ARS
Defecation bouts
0.0187
0.0126
V
C
V
C
V: Vehicle
C: C21
l
hM4Di-EGFP_Vehicle (N=10)
hM4Di-EGFP_C21 (N=9)
EGFP_Vehicle (N=7)
EGFP_C21 (N=7)
Defecation rate (%)
ns
0.0208
Defecation latency (s)
m
hM4Di-EGFP
Time in the center (s)
ns
Vehicle
C21
n
hM4Di-EGFP
Running distance (cm)
ns
Vehicle
C21
o
EGFP
Defecation bouts
ns
Vehicle
C21

Figure 2

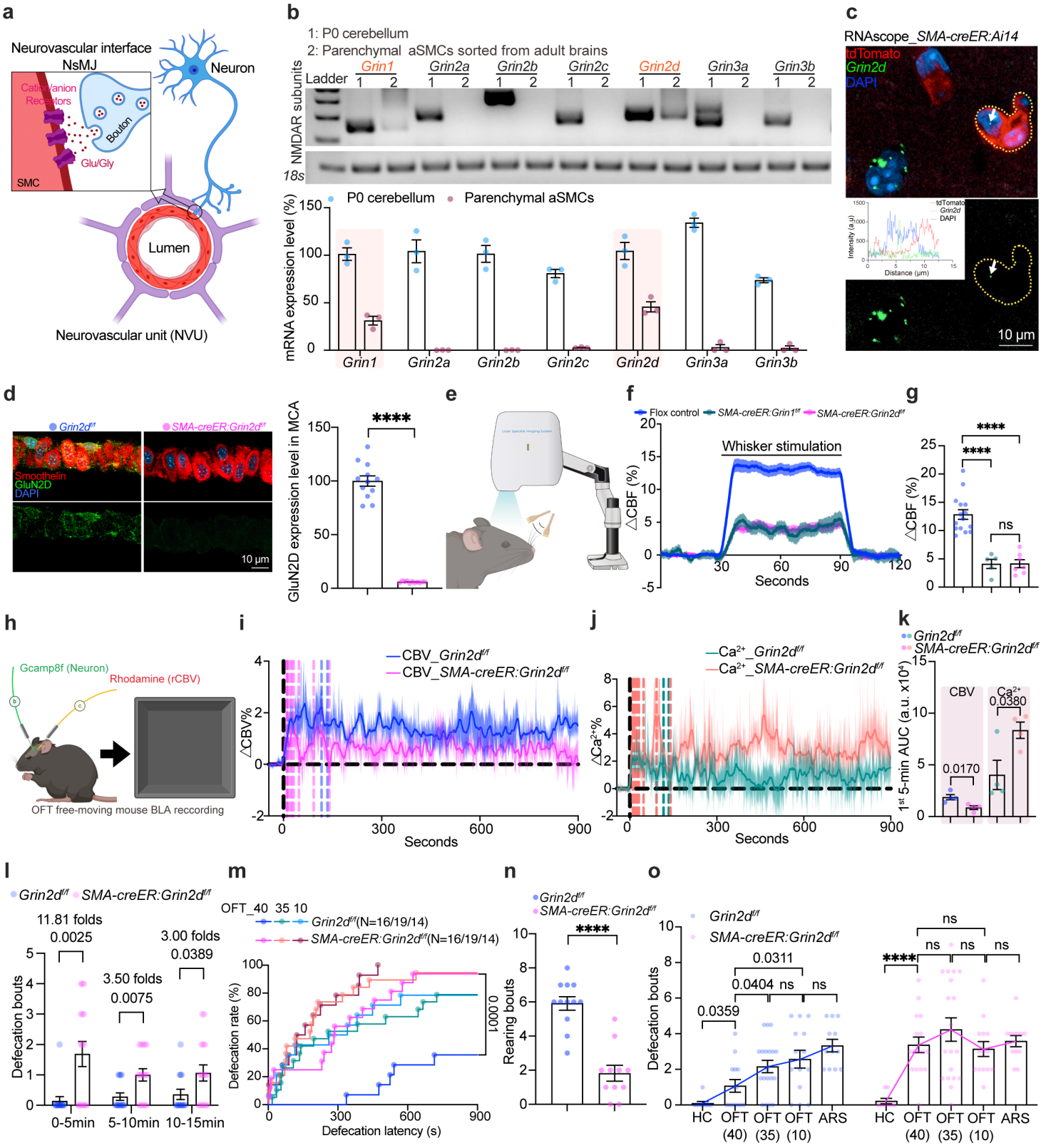
a
Neurovascular interface
NsMJ
Neuron
Cation/anion Receptors
Bouton
Glu/Gly
SMC
Lumen
Neurovascular unit (NVU)
b
1: P0 cerebellum
2: Parenchymal aSMCs sorted from adult brains
Ladder
Grin1
Grin2a
Grin2b
Grin2c
Grin2d
Grin3a
Grin3b
NMDAR subunits
18s
P0 cerebellum
Parenchymal aSMCs
mRNA expression level (%)
c
RNAscope_SMA-creER:Ai14
tdTomato
Grin2d
DAPI
Intensity (a.u)
Distance (μm)
10 μm
d
Grin2d f/f
SMA-creER:Grin2d f/f
Smoothelin
GluN2D
DAPI
10 μm
e
GluN2D expression level in MCA
****
f
Flox control
SMA-creER:Grin1 f/f
SMA-creER:Grin2d f/f
Whisker stimulation
△CBF (%)
Seconds
g
****
****
ns
△CBF (%)
h
Gcamp8f (Neuron)
Rhodamine (rCBV)
OFT free-moving mouse BLA reccording
i
CBV_Grin2d f/f
CBV_SMA-creER:Grin2d f/f
△CBV%
Seconds
j
Ca2+_Grin2d f/f
Ca2+_SMA-creER:Grin2d f/f
△Ca2+%
Seconds
k
Grin2d f/f
SMA-creER:Grin2d f/f
CBV
Ca2+
0.0170
0.0380
1st 5-min AUC (a.u. x10⁴)
l
Grin2d f/f
SMA-creER:Grin2d f/f
11.81 folds
0.0025
3.50 folds
0.0075
3.00 folds
0.0389
Defecation bouts
0-5min
5-10min
10-15min
m
OFT_40 35 10
Grin2d f/f(N=16/19/14)
SMA-creER:Grin2d f/f(N=16/19/14)
Defecation rate (%)
0.0001
Defecation latency (s)
n
Grin2d f/f
SMA-creER:Grin2d f/f
****
Rearing bouts
o
Grin2d f/f
SMA-creER:Grin2d f/f
0.0311
0.0404
ns
0.0359
Defecation bouts
HC
OFT (40)
OFT (35)
OFT (10)
ARS

Figure 3

Ruan et al.

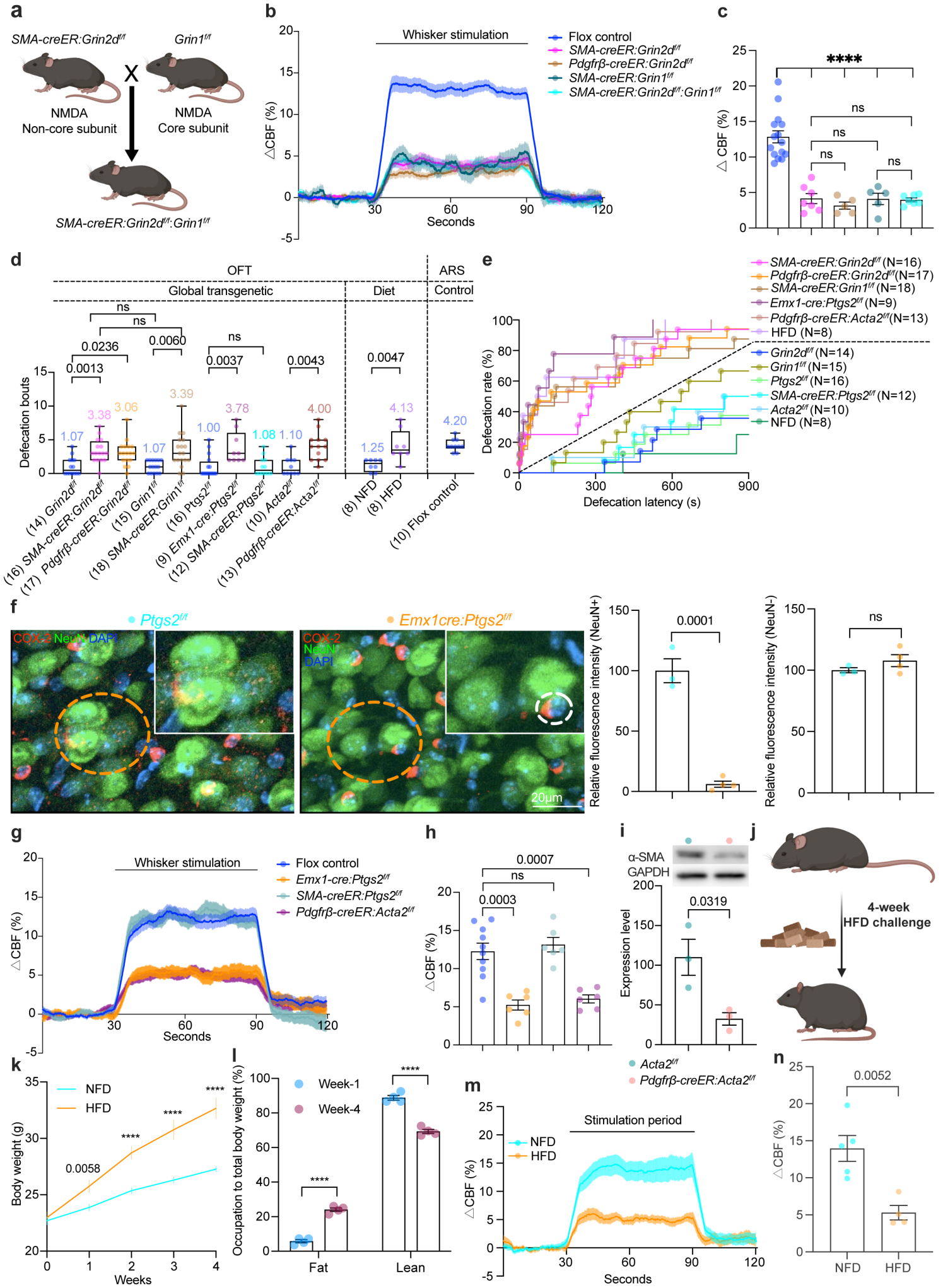

Figure 4

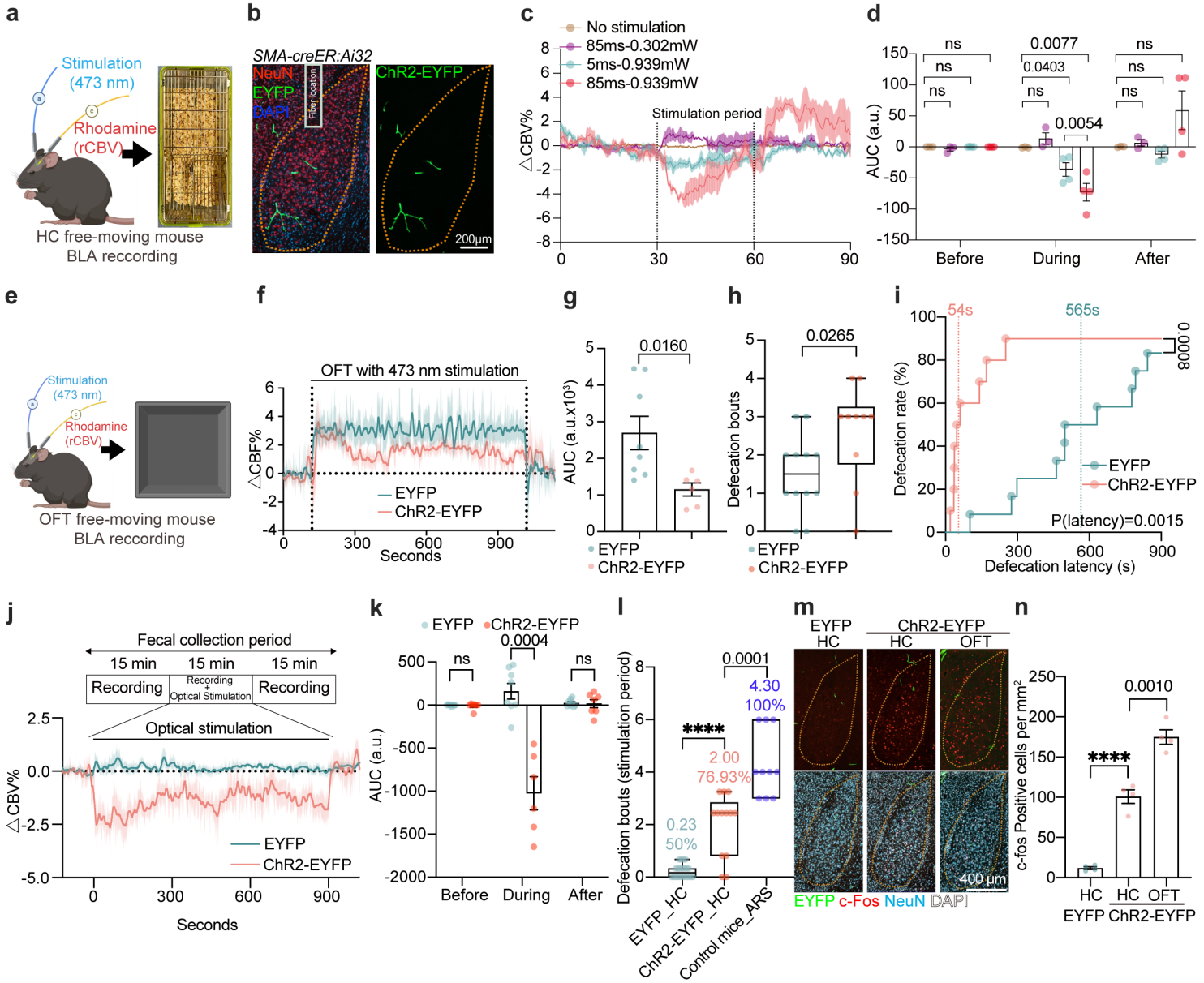
a
Stimulation (473 nm)
Rhodamine (rCBV)
HC free-moving mouse BLA reccording
b
SMA-creER:Ai32
NeuN
EYFP
DAPI
Fiber location
ChR2-EYFP
200μm
c
No stimulation
85ms-0.302mW
5ms-0.939mW
85ms-0.939mW
Stimulation period
△CBV%
d
AUC (a.u.)
ns
0.0077
0.0403
0.0054
Before
During
After
e
Stimulation (473 nm)
Rhodamine (rCBV)
OFT free-moving mouse BLA reccording
f
OFT with 473 nm stimulation
△CBF%
EYFP
ChR2-EYFP
Seconds
g
AUC (a.u.x10³)
0.0160
EYFP
ChR2-EYFP
h
Defecation bouts
0.0265
EYFP
ChR2-EYFP
i
54s
565s
Defecation rate (%)
0.0008
EYFP
ChR2-EYFP
P(latency)=0.0015
Defecation latency (s)
j
Fecal collection period
15 min
15 min
15 min
Recording
Recording + Optical Stimulation
Recording
Optical stimulation
△CBV%
EYFP
ChR2-EYFP
Seconds
k
EYFP
ChR2-EYFP
ns
0.0004
ns
AUC (a.u.)
Before
During
After
l
Defecation bouts (stimulation period)
0.0001
****
0.23
50%
2.00
76.93%
4.30
100%
EYFP_HC
ChR2-EYFP_HC
Control mice_ARS
m
EYFP
ChR2-EYFP
HC
HC
OFT
400 μm
EYFP c-Fos NeuN DAPI
n
c-fos Positive cells per mm²
0.0010
****
HC
HC
OFT
EYFP
ChR2-EYFP

Figure 5

Ruan et al.

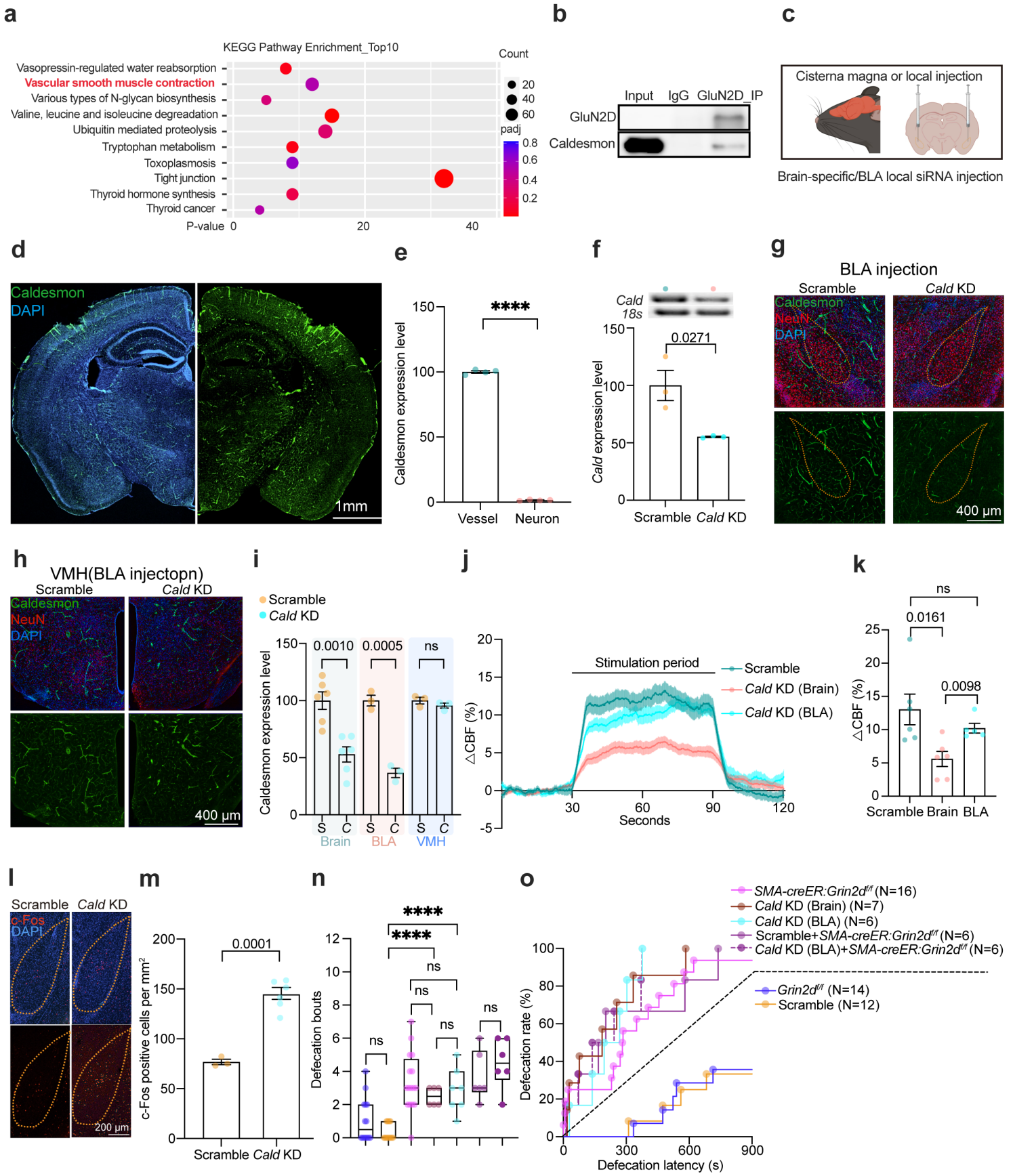

Figure 6

Ruan et al.

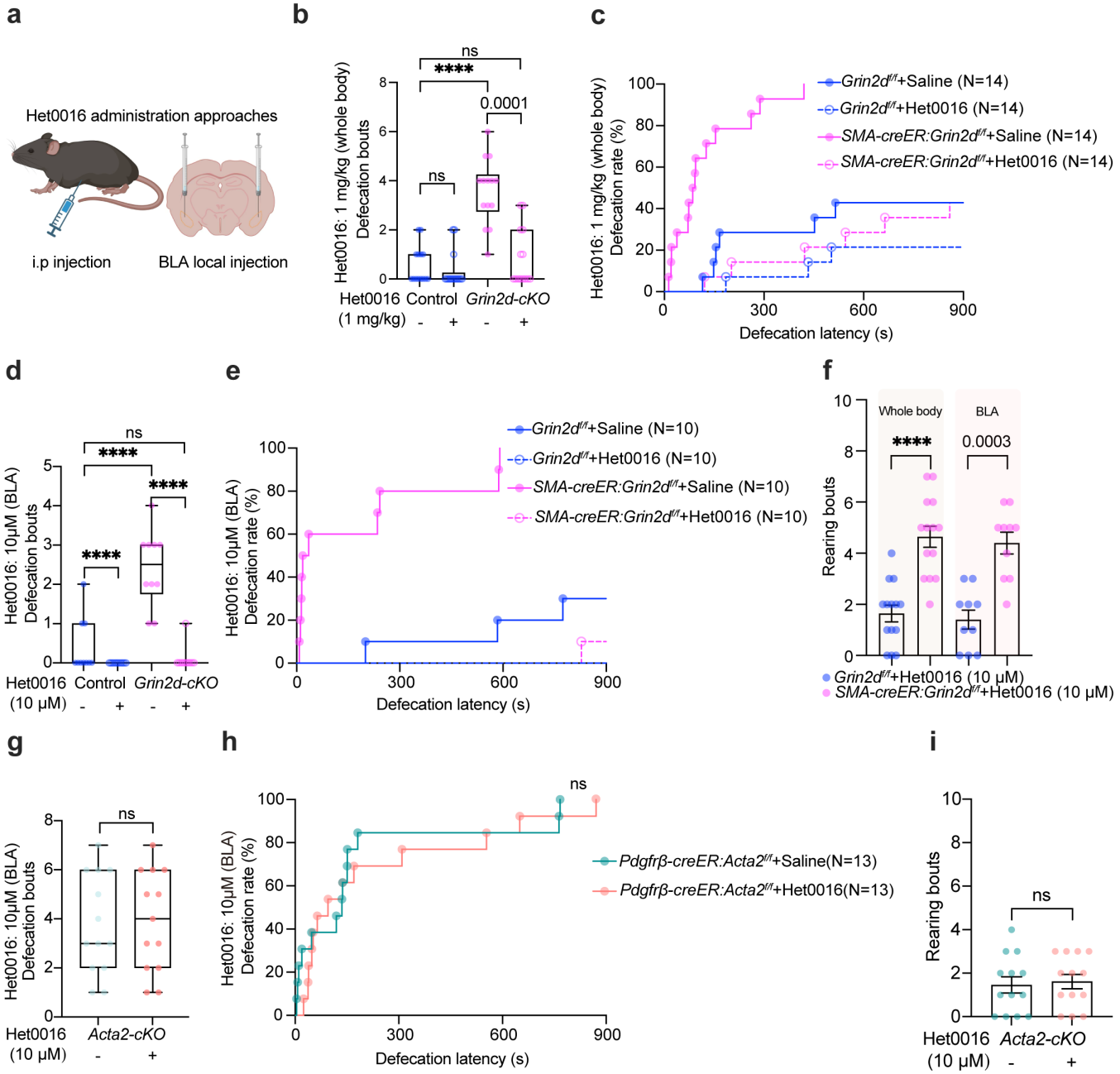

Figure 7

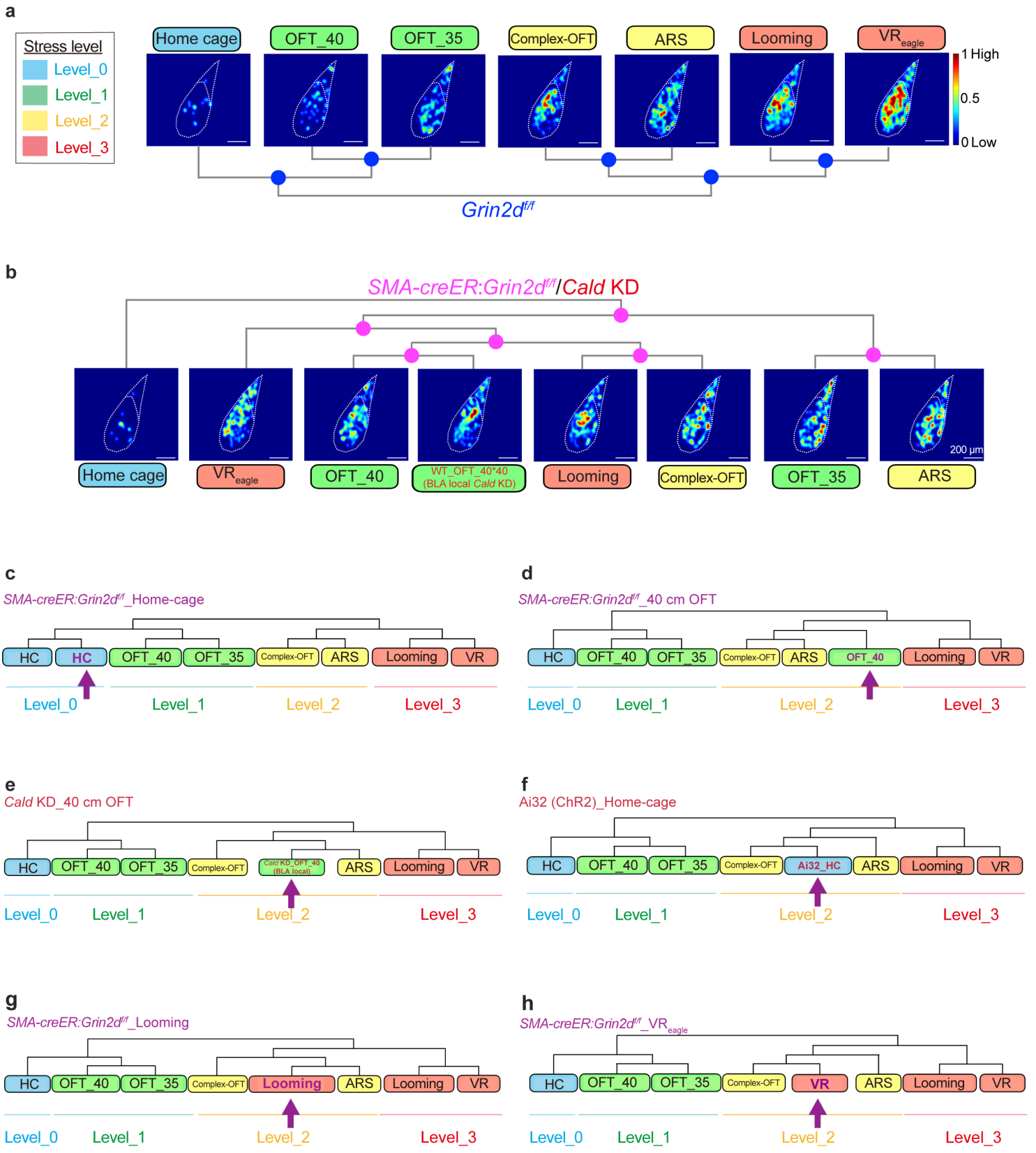
a
Stress level
Level_0
Level_1
Level_2
Level_3
Home cage
OFT_40
OFT_35
Complex-OFT
ARS
Looming
VR eagle
1 High
0.5
0 Low
Grin2d f/f
b
SMA-creER:Grin2d f/f/Cald KD
Home cage
VR eagle
OFT_40
WT_OFT_40*40 (BLA local Cald KD)
Looming
Complex-OFT
OFT_35
ARS
200 μm
c
SMA-creER:Grin2d f/f_Home-cage
HC
HC
OFT_40
OFT_35
Complex-OFT
ARS
Looming
VR
Level_0
Level_1
Level_2
Level_3
d
SMA-creER:Grin2d f/f_40 cm OFT
HC
OFT_40
OFT_35
Complex-OFT
ARS
OFT_40
Looming
VR
Level_0
Level_1
Level_2
Level_3
e
Cald KD_40 cm OFT
HC
OFT_40
OFT_35
Complex-OFT
Cald KD_OFT_40 (BLA local)
ARS
Looming
VR
Level_0
Level_1
Level_2
Level_3
f
Ai32 (ChR2)_Home-cage
HC
OFT_40
OFT_35
Complex-OFT
Ai32_HC
ARS
Looming
VR
Level_0
Level_1
Level_2
Level_3
g
SMA-creER:Grin2d f/f_Looming
HC
OFT_40
OFT_35
Complex-OFT
Looming
ARS
Looming
VR
Level_0
Level_1
Level_2
Level_3
h
SMA-creER:Grin2d f/f_VR eagle
HC
OFT_40
OFT_35
Complex-OFT
VR
ARS
Looming
VR
Level_0
Level_1
Level_2
Level_3

Figure 8

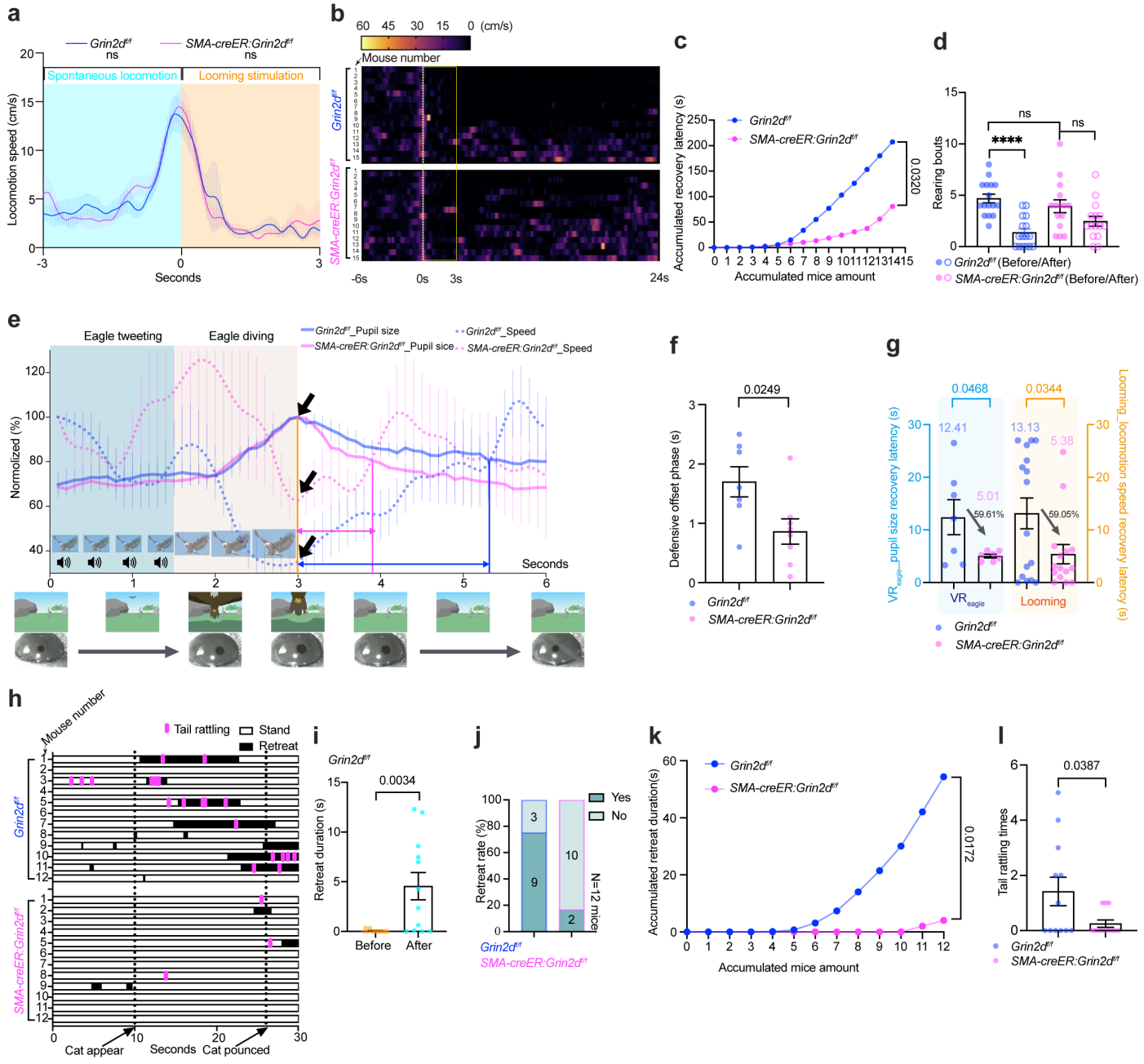
a
Grin2df/f
ns
SMA-creER:Grin2df/f
ns
Spontaneous locomotion
Looming stimulation
Locomotion speed (cm/s)
Seconds
b
60 45 30 15 0 (cm/s)
Mouse number
Grin2df/f
SMA-creER:Grin2df/f
-6s
0s
3s
24s
c
Accumulated recovery latency (s)
Grin2df/f
SMA-creER:Grin2df/f
0.0320
Accumulated mice amount
d
Rearing bouts
ns
****
ns
Grin2df/f (Before/After)
SMA-creER:Grin2df/f (Before/After)
e
Eagle tweeting
Eagle diving
Grin2df/f_Pupil size
Grin2df/f_Speed
SMA-creER:Grin2df/f_Pupil sice
SMA-creER:Grin2df/f_Speed
Normolized (%)
Seconds
f
Defensive offset phase (s)
0.0249
Grin2df/f
SMA-creER:Grin2df/f
g
0.0468
0.0344
12.41
5.01
59.61%
13.13
5.38
59.05%
VReagle_pupil size recovery latency (s)
Looming_locomotion speed recovery latency (s)
VReagle
Looming
Grin2df/f
SMA-creER:Grin2df/f
h
Mouse number
Tail rattling
Stand
Retreat
Grin2df/f
SMA-creER:Grin2df/f
Cat appear
Seconds
Cat pounced
i
Grin2df/f
0.0034
Retreat duration (s)
Before
After
j
Retreat rate (%)
Yes
No
3
9
10
2
N=12 mice
Grin2df/f
SMA-creER:Grin2df/f
k
Accumulated retreat duration(s)
Grin2df/f
SMA-creER:Grin2df/f
0.0172
Accumulated mice amount
l
Tail rattling times
0.0387
Grin2df/f
SMA-creER:Grin2df/f

Figure 9

Ruan et al.

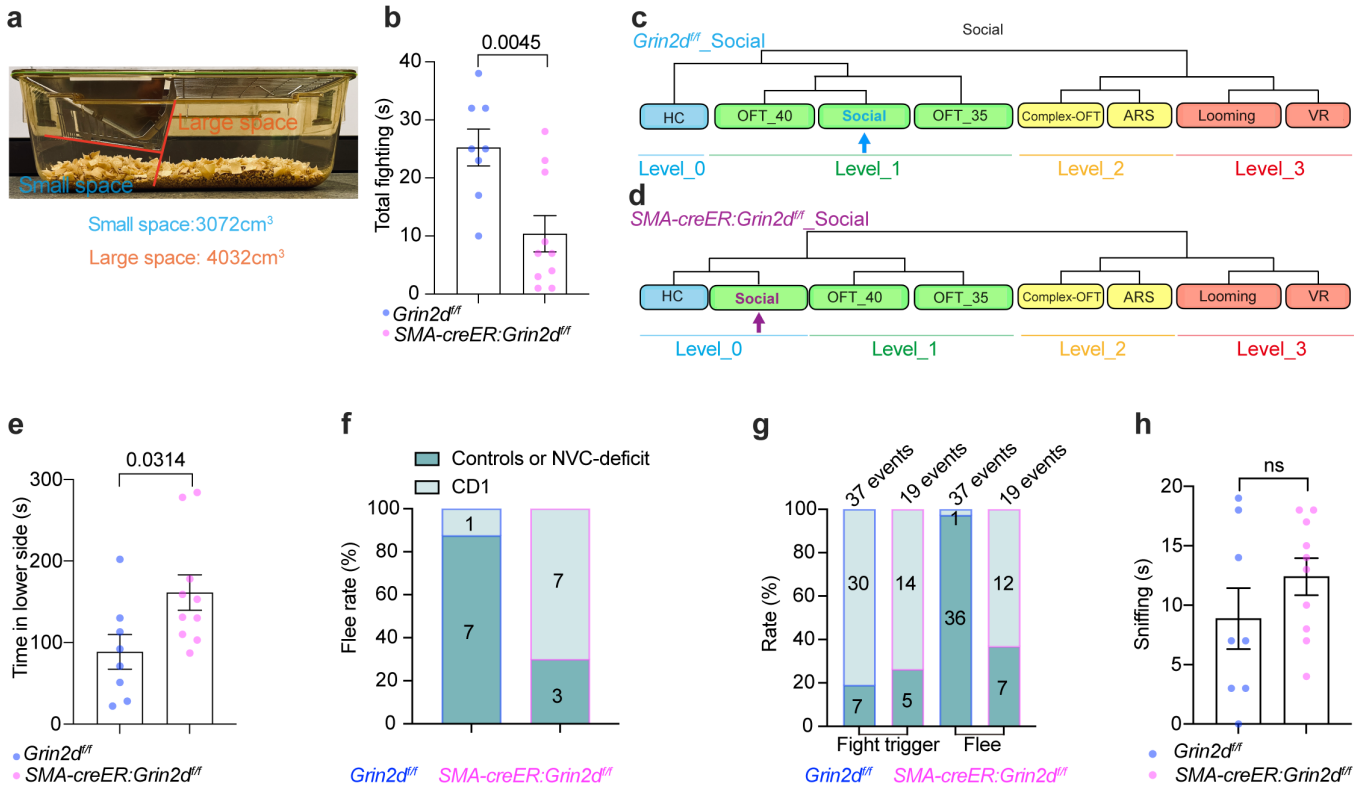

Figure 10
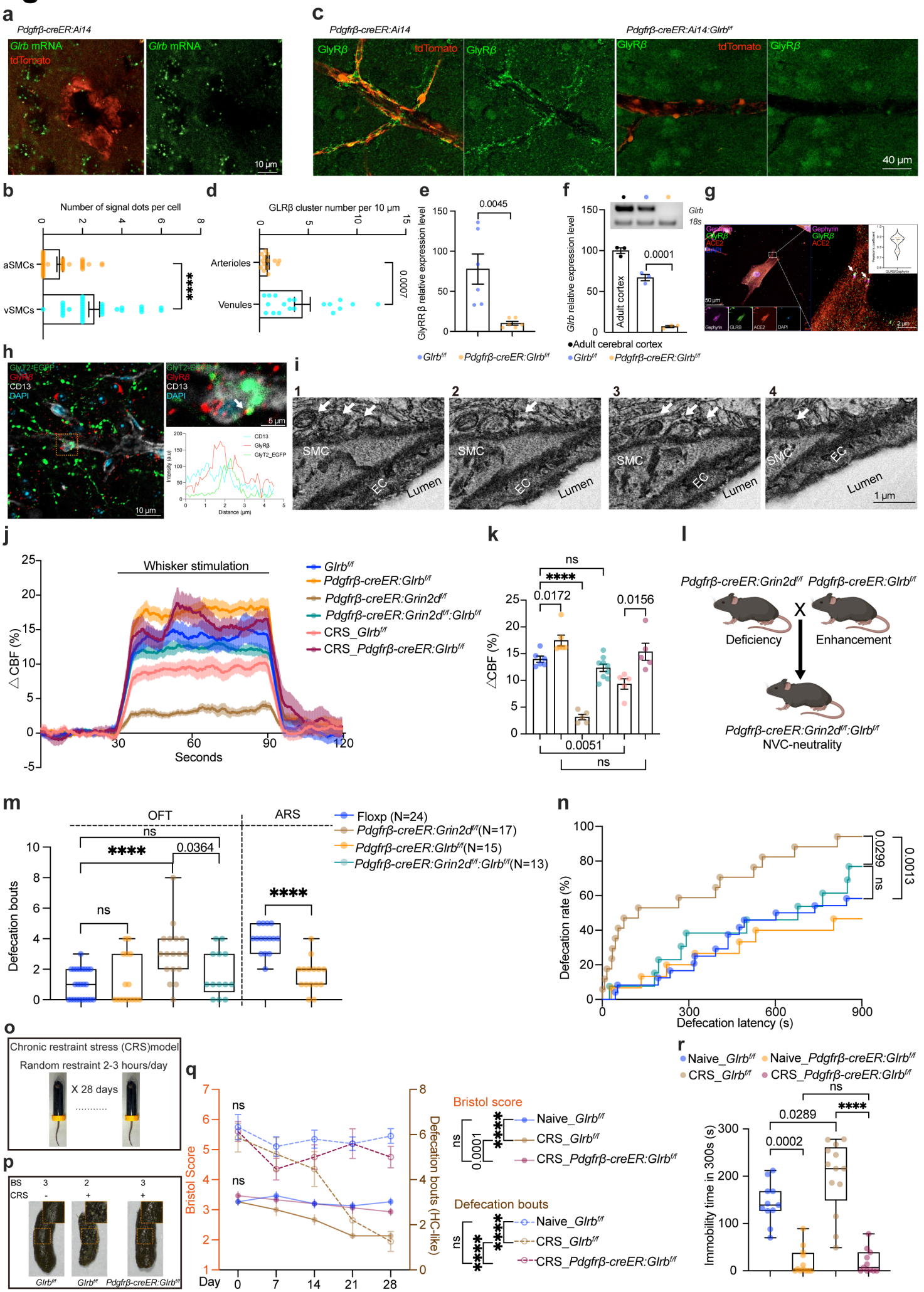
Ruan et al.